JGR Atmospheres

RESEARCH ARTICLE
10.1029/2022JD037268

Key Points:

- Thunderstorms preferentially develop near the center of a misaligned tropical cyclone in the early morning, which can initiate alignment
- Convection reshapes the confluent flow improving boundary layer moisture, increasing vorticity, and begetting more persistent convection
- Cool air from thunderstorm downdrafts create boundaries that can initiate new thunderstorms and eventually form a new center

Correspondence to:
G. R. Alvey III,
george.alvey@noaa.gov

Citation:
Alvey, G. R. III, & Hazelton, A. (2022). How do weak, misaligned tropical cyclones evolve toward alignment? A multi-case study using the Hurricane Analysis and Forecast System. *Journal of Geophysical Research: Atmospheres*, *127*, e2022JD037268. https://doi.org/10.1029/2022JD037268

Received 8 JUN 2022
Accepted 7 OCT 2022

How Do Weak, Misaligned Tropical Cyclones Evolve Toward Alignment? A Multi-Case Study Using the Hurricane Analysis and Forecast System

George R. Alvey III[1,2] and Andrew Hazelton[1,2]

[1]University of Miami/CIMAS, Miami, FL, USA, [2]NOAA/AOML/HRD, Miami, FL, USA

Abstract This study simulates five initially weak, moderately sheared tropical cyclones (TCs) from the 2020–2021 North Atlantic basin hurricane seasons using the Hurricane Analysis and Forecast System (HAFS). Four of the five simulations rapidly evolve from misaligned vortices with asymmetric precipitation and thermodynamic distributions toward more aligned and symmetric configurations. The displaced low-level (LLC) and mid-level circulations (MLC) non-monotonically progress toward alignment with periods of reformation, precession, and advection. Beginning 12–18 hr pre-alignment, TCs have increasingly greater mid-tropospheric humidity and areal coverages of precipitation downshear left than the simulation that fails to align. Alignment precedes the most sustained symmetrization of favorable thermodynamics and precipitation, but deep convection (not necessarily symmetric) plays a critical role in alignment. Ida (2021), a high impact US storm, undergoes a vortex-scale evolution where an increase in areal coverage and intensity of deep convection promotes a reformation of the vortex into a smaller compact core with a closed MLC (a closed LLC does not immediately form). This convective behavior downtilt helps to reshape the irrotational velocity field in the lower troposphere toward the reformed vortex. The increasingly convergent flow of favorable boundary layer thermodynamics within the inflow region thereby increases the instability, which maintains the persistent intense convection. The confluent flow ultimately promotes an advection of the pre-existing LLC toward the reformed vortex resulting in alignment. Tilt reductions are also shown to be temporally linked with the diurnal cycle, wherein convection preferentially increases near the center during the early morning hours (local time).

1. Introduction

After lagging improvements in track forecasts over the last few decades, tropical cyclone (TC) intensity change prediction has recently improved (Cangialosi et al., 2020) led by progress in numerical weather prediction and our fundamental understanding of TC processes. Rapid intensification (RI, defined by an increase in maximum-sustained wind ≥30 kt in 24 hr; Kaplan & DeMaria, 2003), however, still has comparatively poor forecasts (Cangialosi et al., 2020; Fischer et al., 2019; Trabing & Bell, 2020). More than 75% of all RI events initially have intensities of 55 kt or less (Wang & Jiang, 2021; cf., Figure 6). The poor prediction of RI is at least partly linked to these weak, early stage TCs that often have a configuration typically thought of as unfavorable for strengthening—the vortex is misaligned and precipitation is asymmetrically distributed around the surface center due to vertical wind shear (Alvey et al., 2015; S. S. Chen et al., 2006; Corbosiero & Molinari, 2002; Fischer et al., 2018, 2022; Reasor et al., 2004). While many storms do not overcome this configuration, some do and rapidly strengthen; the predictors and processes that differentiate RI versus non-RI storms remain unclear.

Previous literature has described the ramifications of vertical wind shear for TC intensification: The differential wind can advect the mid-upper level vortex away from the surface center causing a horizontal displacement of the upper vortex (Frank & Ritchie, 2001; Jones, 1995). This misalignment can increase susceptibility to dry air entrainment, which detrimentally impacts the thermodynamic environment, inhibits or reduces the precipitation near the inner core (Alland et al., 2021a, 2021b; B. Tang & Emanuel, 2010, 2012), and makes it more difficult for the TC to intensify. A misaligned vortex also induces mid-tropospheric thermal anomalies (cold downtilt; DeMaria, 1996; Frank & Ritchie, 1999; Jones, 1995; Ryglicki et al., 2018) that help force asymmetric precipitation concentrated in the downtilt quadrants (Boehm & Bell, 2021). These tilt induced asymmetries tend to have a net negative effect on TC intensification because they displace the latent heating maxima away from the surface circulation. Ultimately, the asymmetries limit the potential for convection near/within the radius of maximum winds (RMW), which is preferential for intensification from an efficiency perspective (Rogers et al., 2013;

Schubert & Hack, 1982), and the displacement of latent heating from the RMW hinders the inward advection of angular momentum surfaces necessary for intensification (Smith & Montgomery, 2015; Smith et al., 2009). Therefore, achieving a virtually aligned state of the vortex is a critical step toward maximizing potential intensification rates—it promotes a feedback that creates a more symmetric precipitation structure and thermodynamic environment (Alvey et al., 2020; X. Chen et al., 2019), and increases near-center latent heating that intensifies the TC warm core and decreases the central pressure.

Despite the generally accepted importance of alignment for TC intensification, differing pathways toward achieving this state have been shown within the literature. Some modeling studies have shown tilt reduction from a precession of the vortex; a favorable configuration for advection of the mid-level center (MLC) toward the low-level center (LLC) occurs after the tilt vector reaches the upshear left quadrant (Finocchio et al., 2016; Jones, 1995; Munsell et al., 2017; Rios-Berrios et al., 2018). The studies that demonstrate precession, however, often feature slightly more well-developed and less misaligned vortices. On the other hand, other pathways toward alignment have been found associated with weaker and/or more disorganized initial circulations. One such pathway, vortex reformation (Molinari et al., 2006), occurs when a sufficient coverage of intense convection associated with the mid-level vortex induces a new LLC to form via vortex stretching (Rogers et al., 2020). To help simplify the problem, Schecter and Menelaou (2020) analyzed alignment processes in a shear-free environment by artificially inducing tilted vortices in idealized simulations. They noted two preferred scenarios for initial tilt reduction in their simulations: (a) A mid-level vortex core reformation and (b) a diabatically driven surface center migration toward deep convection downtilt. After the initial rapid tilt decrease, transient tilt growth was often observed followed by a gradual reduction until achieving sustained alignment. The results have some similarities with simulations in an ensemble of Edouard (2014) from Alvey et al. (2020), wherein non-monotonic tilt reduction occurred in many members.

Because many early stage TCs can undergo these transitions (sometimes abruptly) from a seemingly unfavorable misaligned vortex toward alignment and RI (X. Chen et al., 2018; Molinari et al., 2006; Munsell et al., 2017; Nguyen & Molinari, 2015), this poses immense challenges for numerical weather prediction and operational forecasting. Although the aforementioned literature has documented the physical processes of vortex alignment, the vortex-scale characteristics governing the differing pathways remain more unclear. In short, this provides motivation for continued understanding in these types of TCs—What are the synergies between the thermodynamic environment and precipitation before, during, and after alignment; and how are they linked to the dynamical processes? This study addresses these questions by using a new state of the art modeling system, and analyzes a series of high-impact cases that underwent rapid transitions from misaligned, weak TCs to rapidly intensifying hurricanes. Through a multi-storm evaluation more robust conclusions can be made about alignment processes as precursors to RI in the early stages of storms.

2. Data and Methods

2.1. HAFS-A Regional Overview

This study uses the Hurricane Analysis and Forecast System (HAFS), which is part of NOAA's Unified Forecast System (UFS). HAFS uses a nested configuration of the finite-volume-cubed-sphere (FV3) dynamical core (e.g., Harris & Lin, 2013). Specifically, the regional-nested version of HAFS (HAFS-A or HAFS-SAR; Dong et al., 2020) is used in this study with the domain boundary demonstrated in Figure 1. This version features a large static nest with 3-km horizontal grid spacing over the North Atlantic basin, with initial and boundary conditions coming from the operational Global Forecast System (GFS). The model uses 91 vertical levels. The model physics configuration is the same as that used in the 2021 real-time Hurricane Forecast Improvement Project (HFIP) runs. HAFS-A uses the 6-class Geophysical Fluid Dynamics Laboratory (GFDL) microphysics scheme (J.-H. Chen & Lin, 2013; Zhou et al., 2019), the scale-aware SAS convective parameterization (Han et al., 2017), and the rapid radiation transfer model for GCMs (RRTMG) radiation scheme (Iacono et al., 2008). For the planetary boundary layer (PBL) physics, HAFS-A uses the eddy diffusivity mass flux with prognostic turbulent kinetic energy (EDMF-TKE) parameterization outlined in Han and Bretherton (2019), which is also currently used in the operational GFS. Similar high-resolution versions of HAFS have been used to study the intensification and evolution of Atlantic TCs such as Hurricane Michael in 2018 (Hazelton et al., 2020) and Hurricane Dorian in 2019 (Hazelton et al., 2021).

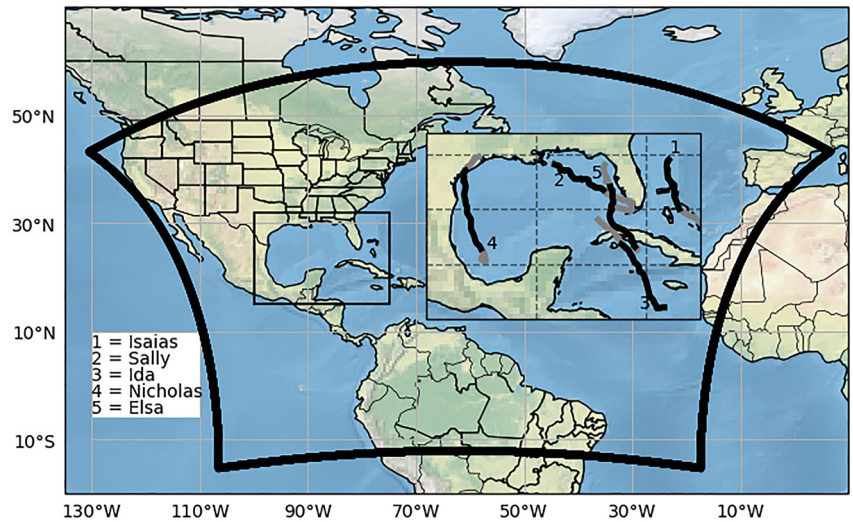

Figure 1. HAFS-A domain outlined by (thick) black with the inset panel depicting a small boxed region covering parts of the Gulf of Mexico, NW Caribbean Sea, and far SW Atlantic. Black track lines (gray lines) within the inset indicate analyzed track periods (unanalyzed simulation periods) in this study including (1) Isaias, (2) Sally, (3) Ida, (4) Nicholas, and (5) Elsa.

2.2. Observational Platforms for Case Identification

Ground-based radar data are processed into Cartesian grids for 2020–2021 Atlantic basin TCs with best track center positions less than 300 km from coastal WSR-88D and Cayman Islands National Weather Service radars. Single Doppler radial velocities and multi-Doppler wind retrievals (for multiple overlapping radars; Bell et al., 2020) allow for TC center determination at different heights and vortex tilt estimates using methodologies described in Alvey et al. (2022) and Section 2.3. Aircraft reconnaissance Vortex Data Messages also provide complementary low-level center position estimates when a ground radar's lowest elevation angle exceeds the height of the lower troposphere, typically at greater distances from the radar site. This observational data, in conjunction with best track intensities, is used for identifying cases to simulate within HAFS and the comparisons shown in Section 3.1.

2.3. Center Finding and Tilt Estimates

The TC center at each model vertical level is objectively identified using a center-finding technique outlined in Fischer et al. (2022). To summarize, this methodology identifies the TC center as the grid point at which the storm-relative tangential wind within 100 km of the storm is maximized after the application of a cost function that weights the radial distance and wind speed of each grid point. Because this center-finding algorithm is applied directly to the high temporal and spatial resolution of the model grid, it often delineates the strongest localized circulation, which may be embedded within a broader scale (parent) circulation. Other center finding techniques like using a pressure centroid, as developed by Nguyen et al. (2014), were tested but tended to produce smoother center position movements and did not capture center reformation events, which are of particular interest to this study.

Vortex tilt is calculated using centers identified at each vertical level and is primarily defined by the differential magnitude between the 2–5 and 2–8-km centers (Alvey et al., 2020; Schecter & Menelaou, 2020). It is important to note that the terminology “tilt” and “misaligned” are used interchangeably throughout this manuscript to describe the horizontal displacement between the objectively identified centers at different vertical levels. Tilt does not necessarily imply a coherent or continuous vorticity column between the two differential levels, and rather, more typically manifests as a discontinuity in the vertical for weak TCs.

3. Results

3.1. Case Overviews and Comparisons to Observations

Five cases from 2020 to 2021 are selected that meet the following three criteria: (a) vortex tilt evolution from misaligned to aligned (tilt <25 km), (b) environment with moderate vertical wind shear (10–20 kt), and (c) relatively weak TC initially (<60 kt). The cases chosen for this study include Isaias (2020), Sally (2020), Ida (2021), Nicholas (2021), and Elsa (2021). The model cycle selected for each storm is subjectively chosen based on the best representation of tilt and intensity evolution compared to observations as described in Section 2.2. Alignment must also occur at least 24 hr after model initialization but no later than 96 hr. Therefore, the cycles chosen are as follows: Isaias, 18:00 UTC 30 July 2020; Sally, 12:00 UTC 12 September 2020; Ida, 00:00 UTC 26 August 2021; Nicholas, 12:00 UTC 12 September 2021; Elsa, 12:00 UTC 5 July 2021. All five of the cases had periods of either high forecast error or large uncertainty noted by forecasters and caused significant impacts in the US (particularly, Ida, a storm that eventually made landfall as a major hurricane; Beven et al., 2022), a key motivating factor for this study. Figure 1 shows the HAFS model tracks for the selected simulations.

Figure 2 demonstrates the HAFS tilt and intensity (defined by maximum sustained surface winds) evolutions using a common timeline with respect to the "alignment time" (0 hr) defined by 2–5-km tilt remaining less than 25 km for greater than 3 hr. This threshold also aligns with the ratio of the tilt to the radius of maximum winds remaining less than 0.75 as in Alvey et al. (2020). For the one case that doesn't sustain an aligned vortex, Elsa (2021), the smallest analyzed tilt is used to define the alignment time. Although the alignment for Isaias in HAFS was about 24 hr quicker than reality (not shown), the HAFS tilt evolution qualitatively follows observations once interpolated to the alignment time. It's important to note the intensity in HAFS for Isaias (Figure 2b) and several of the other simulations (Sally, Figure 2d; Elsa, Figure 2j) is initially lower than the best track by ∼5–10 kt. This is likely attributed to the lack of vortex-scale data assimilation and TC Vitals input into this initial HAFS configuration. TC Vitals represent the operational intensity and position estimates from TC forecast centers used for vortex initialization in numerical models (Bender et al., 2017; Tallapragada et al., 2014). Despite this bias, the qualitative evolution of the best track is closely replicated by HAFS with a relatively steady state or slowly intensifying TC initially, followed by an increase in intensification rates after alignment (0 hr, Figure 2b).

Sally (Figure 2c) had an apparent vortex reformation (Brown, 2020) that resulted in observational tilt estimates decreasing from 100 km to below 20 km in 3–6 hr. Although the HAFS tilt evolution did not capture the abrupt alignment, it did generally depict a reduction in 2–5-km tilt preceding the alignment time. The HAFS-diagnosed 0–8-km tilt is much larger (80–100 km) than the HAFS 2–5 km tilt in the 6–12-hr period preceding alignment (not shown). Both the observations and model show that the burst of intensification (∼20 kt in 12 hr) begins prior to alignment (Figure 2d), during the rapid tilt reduction. This result differs a bit from recent literature (Alvey et al., 2020; Munsell et al., 2017; Rios-Berrios et al., 2016) that highlights cases with alignment prior to RI onset, though there is also precedence in the literature for alignment occurring after RI onset (H. Chen & Gopalakrishnan, 2015).

Ida (2021) has a vortex evolution in HAFS that closely mimics observational estimates from reconnaissance and ground radar; it begins with an initial 2–5-km center misalignment of 60 km (Figure 2e) followed by a rapid transition toward alignment near 0 hr. The most substantial intensification occurs during and shortly after the greatest tilt reduction (Figure 2f). Nicholas (2021) similarly featured a rapid transition from a misaligned vortex toward alignment. The HAFS simulation of Nicholas also features a tilt reduction from 100 to 15 km in less than 12 hr (Figure 2g). These tilt reductions coincide with an increase in intensification in both the best track and model analyzed near-surface wind field. Finally, Elsa (2021) was selected as a null case with an attempted alignment (Figure 2i, 0 hr), however, a series of factors, described later in the manuscript, prevented sustained alignment and subsequent intensification (Figure 2j). For the remainder of this manuscript, Elsa is hereafter referred to as the "failed [alignment] simulation," whereas Sally, Ida, Isaias, and Nicholas are the "successful [alignment] simulations."

3.2. Environmental Characterization

Weak TCs typically become misaligned in the presence of moderate (i.e., 10–20 kt) to strong vertical wind shear (VWS, i.e., >20 kt). Several recent studies, however, have documented some cases that become aligned and undergo rapid intensification, despite the presence of moderate VWS (Alvey et al., 2020, 2022; Hazelton

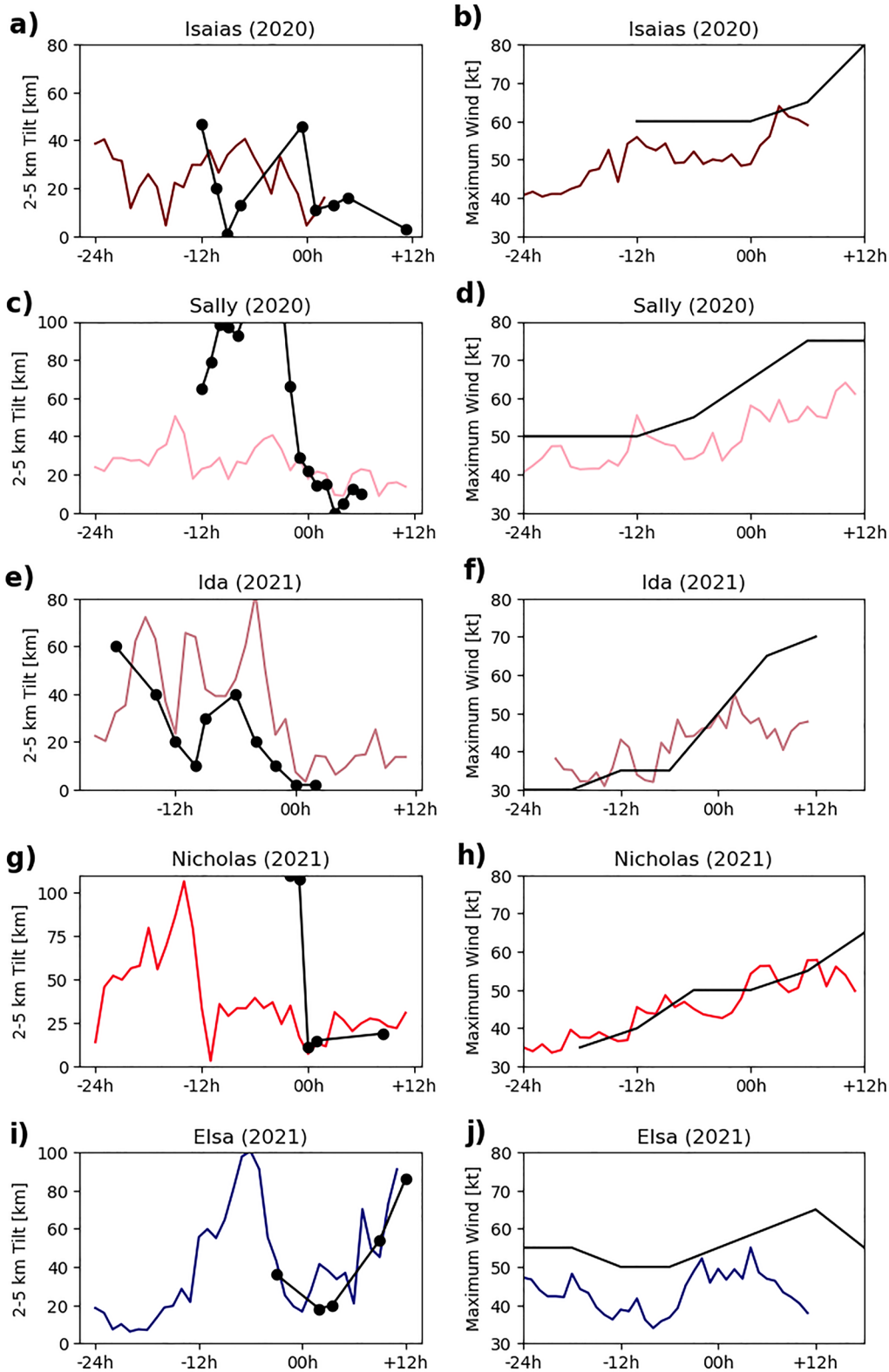
a)
Isaias (2020)
2-5 km Tilt [km]
b)
Isaias (2020)
Maximum Wind [kt]
c)
Sally (2020)
2-5 km Tilt [km]
d)
Sally (2020)
Maximum Wind [kt]
e)
Ida (2021)
2-5 km Tilt [km]
f)
Ida (2021)
Maximum Wind [kt]
g)
Nicholas (2021)
2-5 km Tilt [km]
h)
Nicholas (2021)
Maximum Wind [kt]
i)
Elsa (2021)
2-5 km Tilt [km]
j)
Elsa (2021)
Maximum Wind [kt]
-24h
-12h
00h
+12h

Figure 2.

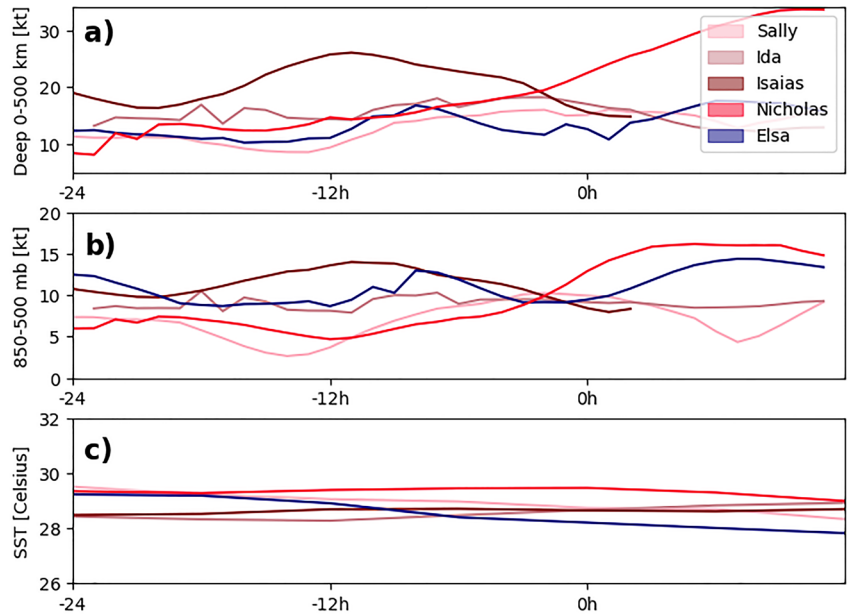

Figure 3. Panel (a) shows 850–200-hPa vertical wind shear (kt) averaged within 0–500 km of the low-level center and with respect to the time of alignment (0 hr) for all simulations as in Figure 2. Panel (b) as in panel (a) except for 850–500-hPa vertical wind shear (kt). Panel (c) demonstrates SST averaged within 200 km of the center for each simulation.

et al., 2020; Rios-Berrios & Torn, 2017; Rios-Berrios et al., 2016; Rogers et al., 2020). In these cases, the vortex overcomes its tilted configuration and asymmetric precipitation distribution, and it transitions toward a more aligned vortex with increases in symmetry and areal coverage of precipitation (and sometimes also the intensity of precipitation). In this study, all five cases examined within HAFS have similar environments characterized by moderate VWS. Figure 3a shows that with the exception of a few time periods, all simulations have deep layer 850–200-hPa VWS values ranging from 10 to 25 kt. Isaias, despite having up to 25 kt of VWS pre-alignment, is able to overcome the detrimental impacts and align. Furthermore, Nicholas successfully sustains alignment in spite of VWS increasing toward 20–30 kt post-alignment. Elsa (Figure 3a, blue line) features some of the lowest VWS values (10–15 kt) indicating that differences in VWS alone were likely not responsible for its failed alignment.

Idealized modeling studies (Finocchio et al., 2016) and individual case studies (Ryglicki et al., 2019) have shown that VWS profiles concentrated more in the upper troposphere may affect TCs and intensity change differently than profiles concentrated in the low-middle troposphere. Therefore, an examination of the vertical depth of wind shear for each simulation is performed (not shown). Mid-level VWS, hypothesized to be more detrimental to early stage TCs (due to shallower vortices and greater dry air entrainment susceptibility; Finocchio et al., 2016), is shown in Figure 3b. Nearly all simulations have VWS values from 5 to 15 kt in the 850–500-hPa layer. Elsa has relatively high mid-level VWS (10–15 kt) compared to its deep layer VWS calculation (12–18 kt), perhaps a factor in its failed alignment attempt that will be explored later in more detail.

The sea surface temperature (SST) is also considered given the dependency of sufficiently high SSTs for convectively driven diabatic processes that can help alignment processes (Schecter, 2022). Figure 3c demonstrates that all simulations had sufficiently high SST (>27.5°C) throughout their life cycles. Sally (2020), Nicholas (2021), and Elsa (2021) had slightly higher SST (>29°C) than Isaias (2020) and Ida (2021) 12–24 hr pre-alignment by ∼1°C. Nicholas maintains the highest SST (>29°C) throughout the simulation period, whereas the other simulations converge near 28.5°C through the −12 to +12-hr period. One exception, Elsa, on the other hand, had the

Figure 2. (a, c, e, g, and i) Two to five kilometers vortex tilt (km) and (b, d, f, h, and j) maximum sustained 10-m wind (kt) for (a and b) Isaias, (c and d) Sally, (e and f) Ida, (g and h) Nicholas, and (i and j) Elsa with respect to alignment time (*x*-axis). Tilt and maximum winds from HAFS simulations are indicated by the color lines (different shades of red for "successful alignment" cases or blue for "failed alignment"). Observations are also plotted in reference to each storm's respective alignment time. Aircraft reconnaissance and ground radar center estimates are used for observational tilt estimates, indicated by the black circles, which are also extrapolated with black lines (a, c, e, g, and i). The best track maximum sustained wind speeds (b, d, f, h, and j) are also indicated by black lines.

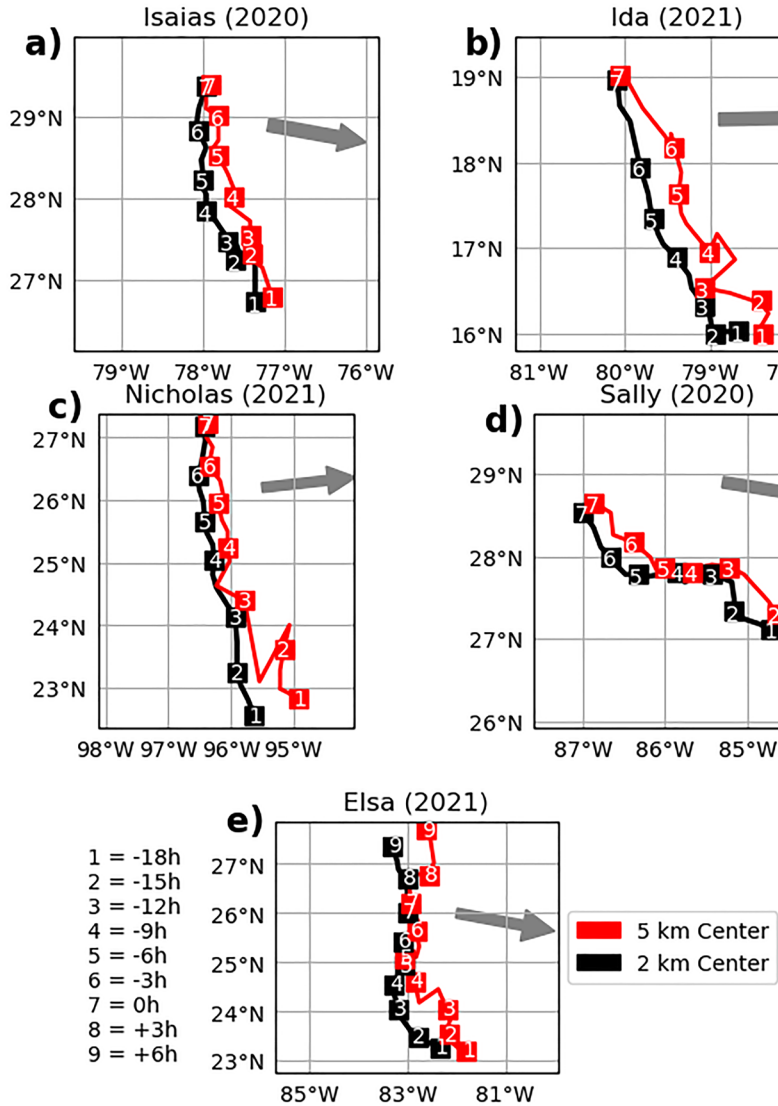

Figure 4. Two-kilometer (black line) and 5-km (red line) center tracks for (a) Isaias, (b) Ida, (c) Nicholas, (d) Sally, and (e) Elsa for the time periods −18–0 hr with respect to alignment (except for Elsa which shows −18 to +6 hr). Each shaded box represents a 3-hr increment with the white number corresponding to the time in the bottom left. The gray arrows indicate the average 850–200-hPa 0–500-km vertical wind shear direction within 6 hr of alignment (0 hr).

lowest SST (~0.5–1°C below the mean) that decreased to <28°C after the attempted alignment, perhaps another factor contributing to the lack of sustained deep convection (shown later in Section 3.4) and an aligned vortex. These subtle environmental differences (with some drastically different outcomes) demonstrate not only the delicate nature of early stage TCs in shear but also the inability of environmental conditions alone to distinguish outcomes. While it is important to consider the environmental conditions given their multi-scale feedback on inner core processes (Hendricks et al., 2010), the remainder of this study will focus on the cooperative interactions between vortex-scale kinematic, precipitation, and thermodynamic processes that help result in alignment.

3.3. Vortex Tilt

The center tracks of both the LLC and MLC in HAFS (Figure 4) reveal important characteristics of the alignment process. Isaias initially only has a tilt magnitude of 20–30 km (Figure 4a), a result of a transient alignment attempt caused by a convective burst (CB, not shown); this evolution is similar to the non-monotonic vortex alignment seen in other modeled weak TCs (Alvey et al., 2020; Schecter & Menelaou, 2020). However, 9–15 hr before

alignment, the tracks of both centers move away from one another as the tilt magnitude increases to 40 km. This is likely due to the influence of persistent moderate wind shear (Figures 3a and 3b) and occurs during a period with decreased convective coverage (not shown). During the period from −3 to 0 hr, the LLC (black line) tracks a much greater distance than the 5-km center, indicating that the LLC either advected toward the MLC or reformed beneath the MLC.

Ida (2021) initially has a greater than 60 km misalignment at −15 hr (Figure 4b). Ida attempts a brief reformation in response to a mesovortex at −12 hr (not shown), however, this transient feature does not persist. Eventually, from −9 to −6 hr the MLC position jumps farther northeast away from the LLC in response to a reforming vortex core followed by an advection of the LLC toward the MLC around −3 hr, which results in alignment. Ida's complex evolution will be examined in more detail in Section 3.5. Nicholas (2021) also begins with a tilt greater than 60 km; the MLC then reforms near the LLC around −15 to −12 hr (Figure 4c). A 20–40-km misalignment remains until the LLC migrates toward the MLC in the 6 hr before alignment. Sally, the final "successful alignment" case examined, initially has a misalignment greater than 40 km at −15 hr (Figure 4d). Between −15 and −12 hr the LLC deviates northward toward the MLC, while the MLC also accelerates toward the NW. Alignment, though, ultimately does not become sustained until precession occurs in the final 6 hr pre-alignment (not shown). Sally is the only case among the storms examined in this study with alignment in HAFS occurring via precession; all remaining "successful alignment" cases feature non-monotonic processes that involve advection and/or reformation of the LLC.

Elsa (2021), the "failed alignment" case, initially has an increasing misalignment that reaches 80 km in the 12–18 hr pre-attempted alignment period. During the following 3–6 hr, the MLC tracks toward the LLC, though some misalignment remains. Finally, near 0 hr (attempted alignment time), the LLC moves slightly closer toward the MLC. The misalignment, however, rapidly grows 3–6 hr post-alignment attempt in the presence of increasing VWS (Figure 3) and a decrease in convective coverage (shown in Section 3.4). Because precipitation and the resultant diabatic effects play an important role in vorticity generation and tilt reduction, Section 3.4 will focus on linking the precipitation structure and intensity to the vortex structural evolution. Section 3.5 will also later address the following unanswered questions: Are these center jumps a result of new vorticity generation beneath the MLC with deep CBs, advective processes, or a combination of both? And how does precipitation govern the physical processes associated with vortex alignment?

3.4. Inner Core Thermodynamic and Precipitation Evolution

3.4.1. Relative Humidity

Zawislak et al. (2016), X. Chen et al. (2019), and Alvey et al. (2020) identified a link between azimuthal precipitation coverage, mid-tropospheric relative humidity (RH), and the increase in symmetrization that often occurs near RI onset. Therefore, Figure 5 first examines the composite of shear relative 600–400-hPa RH for all successful simulations (color shading) and the failed alignment case, Elsa (blue line contours). Initially, at 24 hr prior to alignment (Figure 5a), mid-tropospheric RH values >80% remain primarily confined to the downshear left quadrant (DSL) with very dry air (RH < 50%) dominating the upshear left quadrant (USL). The failed simulation (Elsa), on the other hand, has a much greater inner core areal coverage of RH values >80% (solid blue line contour) during this period, which likely at least partly reflects the initially low tilt magnitudes (Figure 2i) prior to traversing Cuba. During the −24 to −12 hr period (Figure 5b), the areal extent of relatively high RH (>80%) more than doubles in successful simulations; and the magnitude of 600–400-hPa RH significantly increases DSL. This result indicates that humidification in the downshear quadrants, likely associated with precipitation near the MLC, is a key factor in cases that progress toward alignment. By contrast, as the 2–5-km tilt rapidly increases (Figure 2i) in Elsa from −24 to −12 hr, the high RH (>80%) coverage has decreased during this period, particularly within the inner core near the center. The low RH region (<40%, dashed blue contour) has also increased and propagated nearer to the LLC upshear in Elsa, covering a much greater areal extent than the successful simulation composite.

From −12 to 0 hr, the coverage of RH >80% in the successful simulation composite does not significantly change (Figure 5c), however, the maximum values propagate farther into the USL quadrant near the center. This likely reflects the decrease in tilt magnitudes (Figure 2) seen during this period. Despite alignment, the highest RH values still remain mostly confined to DSL at 0 hr, a result similar to Alvey et al. (2020). The USL RH values

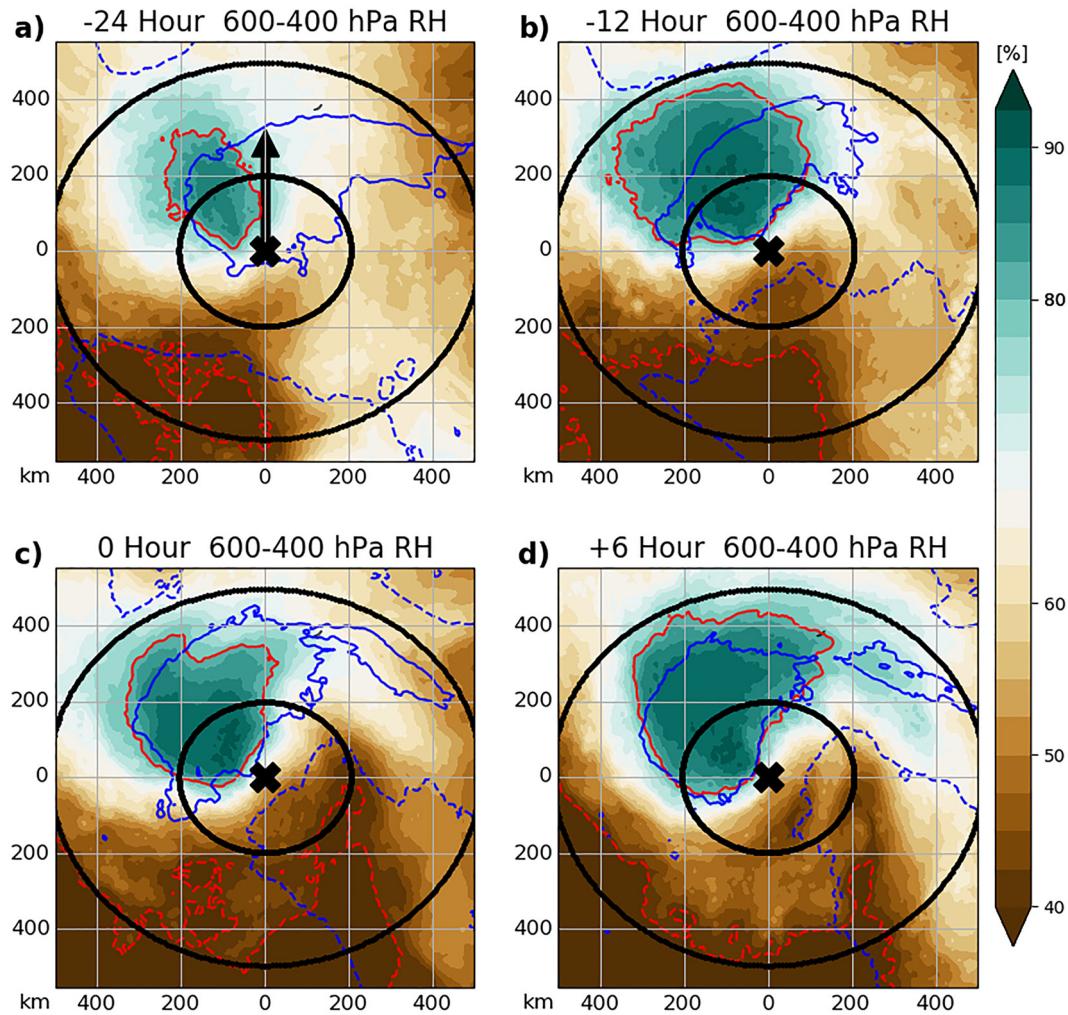

Figure 5. Composite of 600–400-hPa relative humidity (RH, %) rotated with respect to an upward pointing shear vector for all successful simulations: Isaias (2020), Sally (2020), Ida (2021), Nicholas (2021) at (a) −24 hr, (b) −12 hr, (c) 0 hr, and (d) +6 hr with respect to alignment time. The solid (dashed) red line denotes the 80% (40%) contour interval for the composite RH of all successful simulations. The solid (dashed) blue line indicates the 80% (40%) contour interval of shear-relative RH for the same time periods in Elsa (2021). Range rings are 200 and 500 km from the 2-km center and gray grid boxes are spaced 2° latitude and longitude.

increase more appreciably only after alignment in the 6 hr following (Figure 5d), as this aligned configuration provides a more efficient pathway for moisture and precipitation advection into the upshear quadrants. In Elsa, the areal coverage of high RH (solid blue contour) increases again from −12 to 0 hr (Figure 5c), and actually covers a slightly greater area than in the successful composite, including USL. After alignment (+6 hr, Figure 5d), the successful composite and Elsa have fairly comparable distributions of high RH left of shear; however, low RH values in Elsa (dashed blue contour) cover a much larger area right of shear and extend closer to the LLC. Later sections will show that the interaction of this unfavorable, dry mid-tropospheric air with the inner core of Elsa was likely one of the key features that caused the lack of persistent alignment.

3.4.2. Precipitation Partitioning

To examine the connection between precipitation and humidity, the precipitation types are delineated as either stratiform or convection using the Steiner et al. (1995) algorithm, also outlined in Alvey et al. (2020, 2022) and Rogers et al. (2020). Stratiform precipitation can play an important role in not only helping to strengthen the mid-level circulation (Bell & Montgomery, 2019), but also to humidify the mid-troposphere (Alvey et al., 2020; Raymond, 2012), which can eventually provide a more conducive thermodynamic environment for the longevity

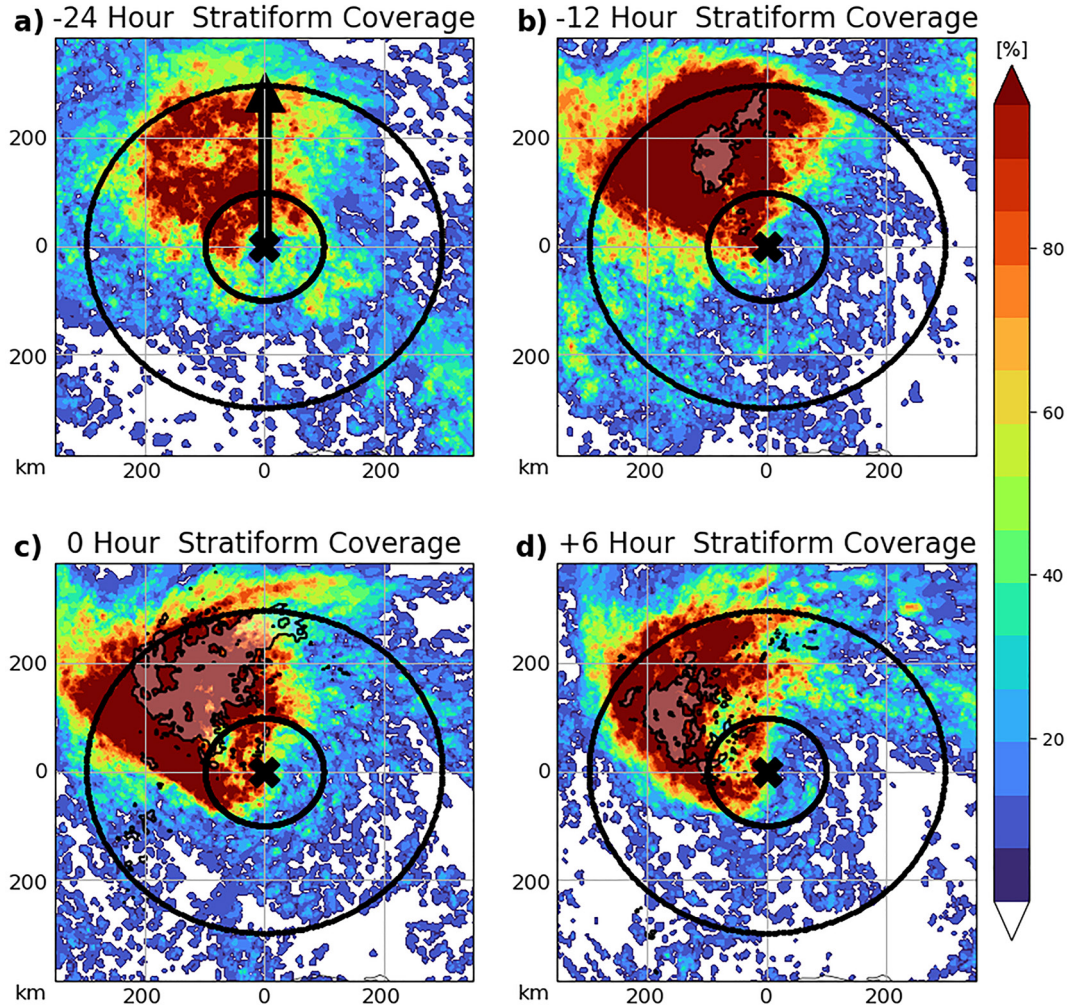

Figure 6. Mean stratiform frequency distributions (%) in the 6-hr period surrounding (a) −24 hr, (b) −12 hr, (c) 0 hr, and (d) +6 hr with respect to alignment. The successful simulations (color shading) and failed simulation (black line contour, 75% interval) are centered on the 2-km center (black *X*) and rotated with respect to the shear vector pointing up. The black circles indicate 100 and 300-km radius.

of future precipitation. Therefore, the frequency distribution of stratiform is calculated over a 6-hr period for each simulation by calculating the percentage of analyses (one-hourly) during that 6-hr period that have precipitation delineated as stratiform at each grid point. Figure 6 demonstrates this frequency distribution in a shear-relative framework averaged for all successful simulations (color shading) and the failed simulation (Elsa, black line contour). Much like the RH distribution in Figure 5, stratiform precipitation dominates DSL during the 24-hr pre-alignment period (Figure 6a). By −12 hr the azimuthal distribution of stratiform remains relatively unchanged, however, the areal extent of >95% distribution has radially expanded. By contrast, the coverage of stratiform in Elsa is significantly smaller in the DSL quadrant.

At the alignment time (0 hr), the coverage of stratiform precipitation still dominates the DSL quadrant (Figure 6c). Unlike the RH, though, it propagates farther into the USL quadrant within 100–150 km of the center. This result reveals that increases in stratiform precipitation USL near alignment precede the humidification in that quadrant by 6–12 hr, indicating the important role that stratiform plays in creating a humid, more favorable environment for sustained precipitation symmetry (Alvey et al., 2020). The stratiform increases seen USL in successful simulations sustain themselves in the 6-hr period following alignment (Figure 6d), however, they remain confined to radii >50 km. The stratiform precipitation in the failed simulation contrastingly remains confined DSL (Figure 6d).

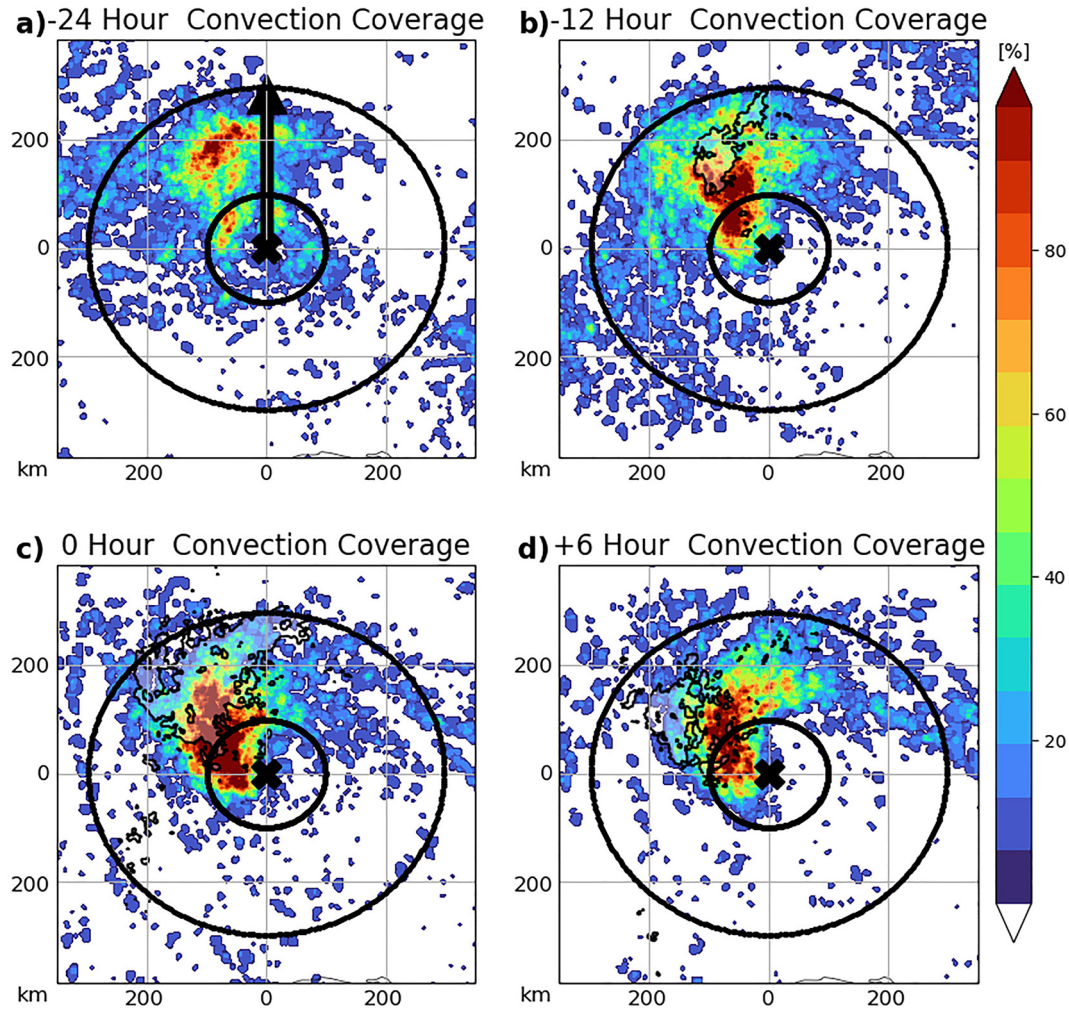

Figure 7. Convection frequency distributions (%) over the 6-hr period surrounding (a) −24 hr, (b) −12 hr, (c) 0 hr, and (d) +6 hr with respect to alignment. The mean percentages of all successful simulations (color shading) and failed simulation (line contour, 75% interval) are centered on the 2-km center (black *X*) and rotated with respect to the shear vector pointing up. The black circles indicate the 100- and 300-km radius.

In addition to the stratiform evolution, it is also important to consider the roles of convection given that stratiform typically emanates from the maturation of convective processes. Figure 7 shows that the areal coverage of convection (of all depths) in successful simulations increases and propagates radially inward closer toward the TC center DSL during the −24 (Figure 7a) to −12 hr (Figure 7b) period. The coverage of convection in Elsa (line contour), on the other hand, is smaller and farther displaced from the TC center at −24 to −12 hr. By 0 hr (Figure 7c), although the frequency of convection in the successful simulations increases slightly and the maximum propagates farther left of shear, coverage in the USL remains significantly less than stratiform precipitation. Because stratiform often represents the maturation of convective processes (Houze, 1997, 2004), it likely has a greater longevity and ability to persist as cyclonic flow advects it USL. By +6 hr the areal coverage of convection actually decreases slightly in successful simulations (Figure 7d), perhaps a similar result to the reductions in the strongest convection found in some previous studies near RI onset (e.g., C. Tao & Jiang, 2015; D. Tao & Zhang, 2019). Much like the stratiform evolution in Elsa, the coverage of convection remains confined to the DSL quadrants, a result of the failure to maintain alignment.

3.4.3. Precipitation Intensity

Several observational and modeling studies have shown the importance of the areal coverage of deep convection to encourage reformation or center repositioning processes (Alvey et al., 2022; Nguyen & Molinari, 2015; Rogers

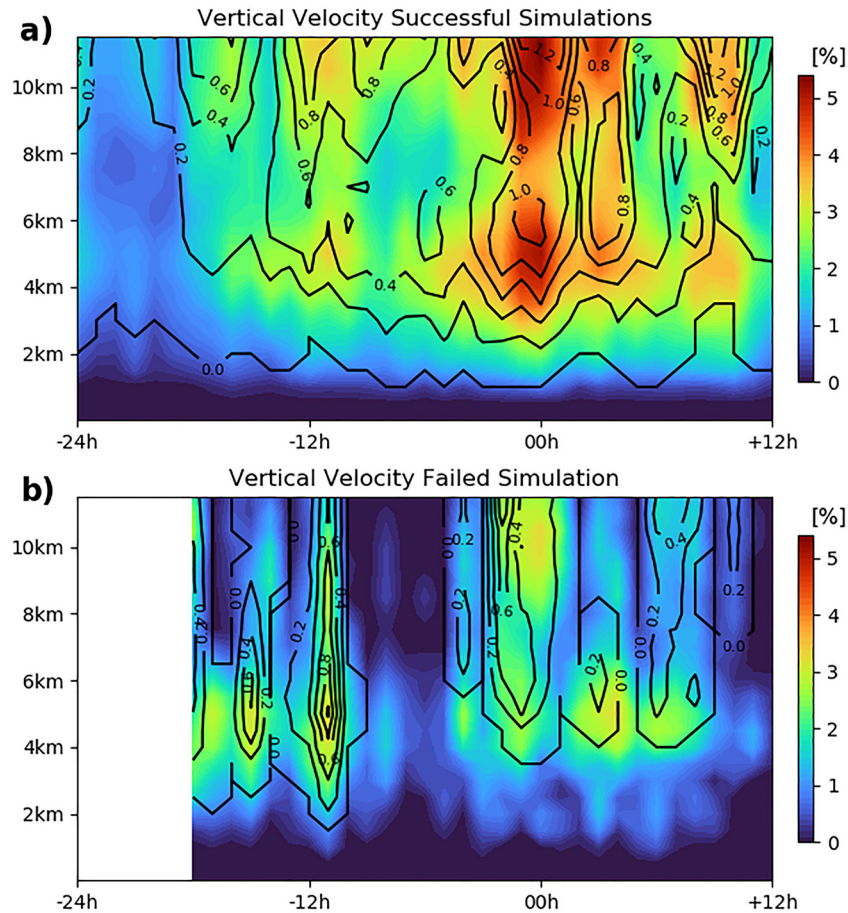

Figure 8. Hovmöller of the average areal coverage of vertical velocity >2 m/s (shading) and >5 m/s (line contour, 0.2-m/s interval) with respect to height within 100 km of the 5-km center for all (a) successful simulations and the (b) failed simulation. The timing on the *x*-axis represents the alignment time (0 hr).

et al., 2016; Schecter, 2020); however, more uncertainty surrounds the importance of convective intensity. Case studies of weak, sheared TCs by Molinari et al. (2006) and Nguyen and Molinari (2015) demonstrated that intense mesovortices can induce abrupt pressure drops and vortex reformations that result in tilt reductions. On the other hand, larger composite satellite studies have concluded that the most intense convection in TCs is not unique to RI cases (Alvey et al., 2015; Fischer et al., 2018; C. Tao & Jiang, 2015).

To elucidate the role of deep convection in alignment, Figure 8 shows a Hovmöller of the areal coverage of vertical velocity >2 m/s (moderate convection, shaded) and >5 m/s (intense convection, line contours) within 100 km of the mid-level center to examine these discrepancies. Figure 8a shows that the frequency distribution of both moderate and intense convection increases beginning ∼18 hr before alignment. The episodic nature of the convective bursts are also reflected by the non-monotonic tilt progression in Figure 2. The greatest increases in both vertical velocity thresholds occur in the final 3–6 hr prior to alignment, wherein the coverage of vertical velocity (w) > 2 m/s increases from 1% to 3% to >4–5% above 3 km and w > 5 m/s increases from ∼0.4% to >1% in the mid-upper troposphere. The failed simulation (Figure 8b) comparatively has similar episodic convective behavior, though the maxima of w > 2 m/s generally don't increase above 3%; and though w > 5 m/s does briefly reach 1%, the coverages and duration are far less than successful simulations. Both of the vertical velocity thresholds generally peak near alignment in the successful simulations and gradually decrease thereafter throughout symmetrization and subsequent intensification. These results indicate the importance of both the intensity of convection and its areal coverage for successful alignment events.

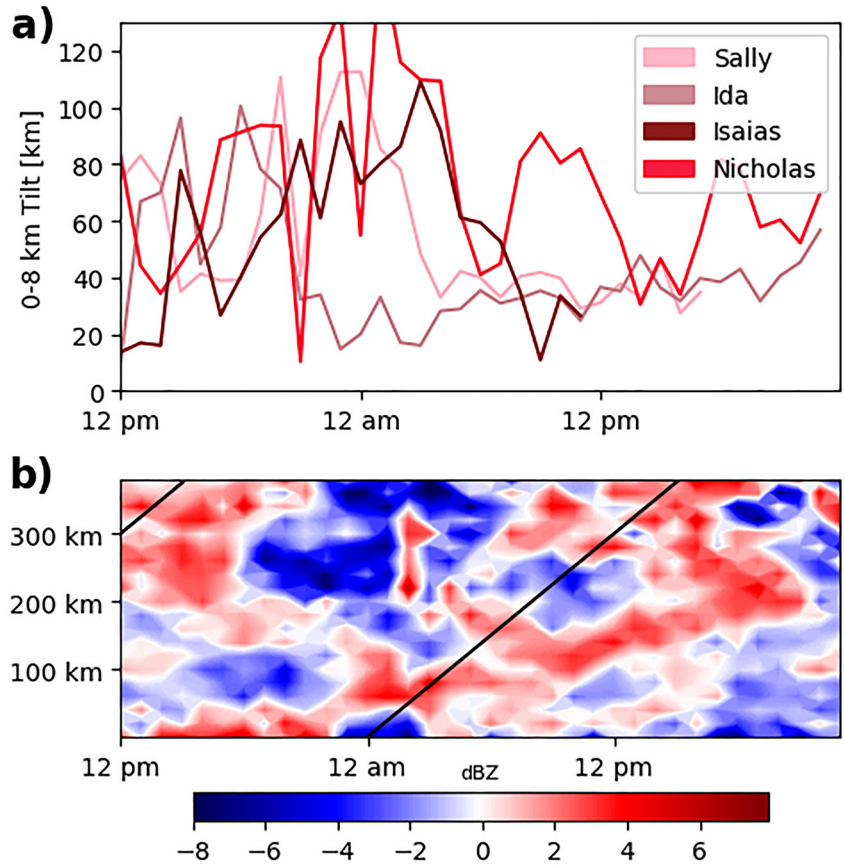

Figure 9. Zero to eight kilometers vortex tilt (km) calculated for all successful simulations with respect to Local Time (top panel, a). A Hovmöller (bottom panel, b) shows the anomaly from the mean of the azimuthally averaged radar reflectivity [dBZ] at each radial distance from the 5-km center and with respect to local time. The black line indicates an extended version of the Dunion et al. (2014) diurnal clock, as in Ditchek, Molinari, et al. (2019).

3.4.4. Diurnal Cycle

Because convection plays such a pivotal role in alignment processes of weak TCs, we also consider the effects of the diurnal cycle. Convective maxima in tropical marine environments have long been observed during morning hours (Gray & Jacobson, 1977; Nesbitt & Zipser, 2003) resulting from the tropical oceanic diurnal cycle. Dunion et al. (2014) more recently identified a TC diurnal pulse wherein inner core cloud tops initially cool in the early morning hours followed by an expansion of cold cloud tops toward outer radii during the afternoon (when cloud tops warm radially inward toward the TC center). Ditchek, Corbosiero, et al. (2019) found that the frequency of diurnal pulses decreased with decreasing TC intensity, however, long-lived pulses were still identified nearly half of the time in tropical storm strength TCs (35–64 kt). Considering the diurnal cycle's impact on convection (Zhang & Xu, 2021), we pose the following question: Does the modulation of precipitation by the diurnal cycle have an effect on the timing of vortex alignment in early stage TCs?

In order to answer this, all HAFS simulations are temporally standardized by local time (LT). Figure 9 shows the precipitation and tilt evolutions of the four successful cases with respect to LT. The tilt of all cases tends to increase during the PM hours (Figure 9a), a time when the diurnal pulse typically causes precipitation to increase in the outer radii (Figure 9b). Tilt magnitude maximizes between 10 p.m. and 3 a.m. in three out of the four cases followed by an abrupt tilt reduction that typically occurs sometime between 12 a.m. and 9 a.m. The tilt reduction in these cases coincides with the diurnal maximum, when inner core convective activity commonly maximizes. This relationship demonstrates a preferential alignment time during the early morning hours. Ida follows a similar sinusoidal-like pattern, however, its tilt maximizes ~6-hr earlier at 6 p.m. before abruptly decreasing and reaching a minimum near 12 a.m. The diurnal pulse signal is also immediately apparent in the radar reflectivity

(Figure 9b), wherein radii >200 km from the center tend to see increases in reflectivity that maximize during the afternoon and evening hours. Precipitation near the center, on the other hand, maximizes during the late p.m. to early a.m. times, slightly preceding the periods of greatest tilt reduction. While not necessarily true of all cases, the results here demonstrate that deep convection preferentially increases near the MLC (within ∼100 km) during the early morning hours, and corresponds with a reduction in vortex tilt. Although several previous studies have similarly demonstrated the importance of the diurnal cycle in early stage TC development and intensification (Dunion et al., 2019; Ruppert et al., 2020; X. Tang & Zhang, 2016), this study also reveals the potential usefulness of local time as a predictor of tilt (in the context of other environmental factors). This is also consistent with recent observational cases, Dorian (2020) and Sally (2020), during which convective bursts led to center reformations during the early morning hours (Alvey et al., 2022; Brown, 2020). Section 3.5 will utilize customized high resolution output from a HAFS simulation of Ida (2021) to investigate the vortex-scale processes responsible for alignment and their relationships to the precipitation evolution.

3.5. Detailed Examination of Vortex Alignment Processes in Ida (2021)

3.5.1. Ida's Vortex Structure and Precipitation Evolution

This section examines the rapid structural change as Ida organized from a misaligned TC to a vertically aligned system in 6–12 hr (Figure 2e). Figure 10a shows the relative vorticity cross-section from the LLC to the MLC and indicates a ∼70–80-km horizontal displacement at −4 hr. The LLC is tilted ∼60 km to the north-northeast (Figures 10a and 10c), whereas the MLC is collocated with a newly reformed vertical vortex. Nearly all of the precipitation remains asymmetric relative to the LLC with deep convection displaced downtilt near the MLC and reformed vortex (Figures 10a and 10c). Just 4 hr later, however, the LLC and MLC have a much more coherent vertical alignment (Figures 10b and 10d) and the reformed vortex has increased greatly in size (vorticity magnitudes $>80 \times 10^{-5}$ s^{-1} extend ∼30 km across horizontally from 0 to 8 km) and strength. The precipitation structure also exhibits a more symmetric distribution with reflectivity values >40 dBZ on average throughout the troposphere. How does Ida's structure transform so rapidly from an asymmetric, misaligned vortex structure to one that is aligned with rapidly increasing symmetry? What events led to the reformation of a new vortex? And what role did the vortex reformation play in alignment?

Ida's vortex alignment can also be demonstrated using horizontal plan view plots of vorticity and storm-relative streamlines at different vertical levels in Figure 11. Figure 11a shows that Ida has a concentrated 2-km vorticity maximum and associated LLC (black *X*) displaced ∼50 km SW of the 5-km MLC (red *X*) 8 hr before alignment. The LLC is located on the SW edge of the precipitation field (Figure 11e), and although the MLC is embedded within a region of convection, the most intense convection (>55 dBZ) is located ∼60 km ENE of the MLC. In the following 2 hr, the convective coverage and center configurations remain similar (Figures 11b and 11f). At −5 and −4 hr the MLC position jumps (Figures 11g and 11h red line) toward the most concentrated and intense convection in response to a reforming low-mid tropospheric vorticity core (also demonstrated by Figure 10a); this region of convection can be traced back to the convective development initially identified 50 km ENE of the MLC that advected northward within the cyclonic flow. Despite an amplifying low-level positive vorticity anomaly (Figure 11d) beneath this new MLC position, a new, closed LLC has not yet reformed and the MLC jump from its previous position has resulted in a 2–5-km tilt increase from ∼50 to 80 km. In the next 2 hr, however, the LLC and associated 2-km vorticity maximum accelerates rapidly NNW toward the newly reformed, compact vorticity core (Figures 11i, 11j, 11m, and 11n), which results in a rapid tilt reduction from ∼75 to ∼25 km. A combination of vorticity maxima mixing, mergers from the advected LLC, and additional formation at 2 km beneath the MLC, results in vortex alignment between −1 and +0.5 hr (Figures 11k and 11l), after which the precipitation begins to rapidly symmetrize (Figure 11p).

Although Figure 11 clearly demonstrates a northward jump of the MLC and subsequent movement of the vorticity at 2 km toward the MLC, the following questions have yet to be addressed: Is the horizontal vorticity advection in the lower troposphere critical to the formation of a vertically aligned vortex? And what promoted the rapid northward movement of the LLC toward the MLC? To begin answering these questions the flow is broken down into rotational and irrotational wind components using a Helmholtz decomposition, as in Ryglicki et al. (2020). Similar to an idealized modeling study by Schecter and Menelaou (2020), we hypothesize that an increase in both the areal coverage and intensity of deep convection downtilt helps reshape the rotational and irrotational velocity field in such a way that promotes the migration of the LLC toward the MLC.

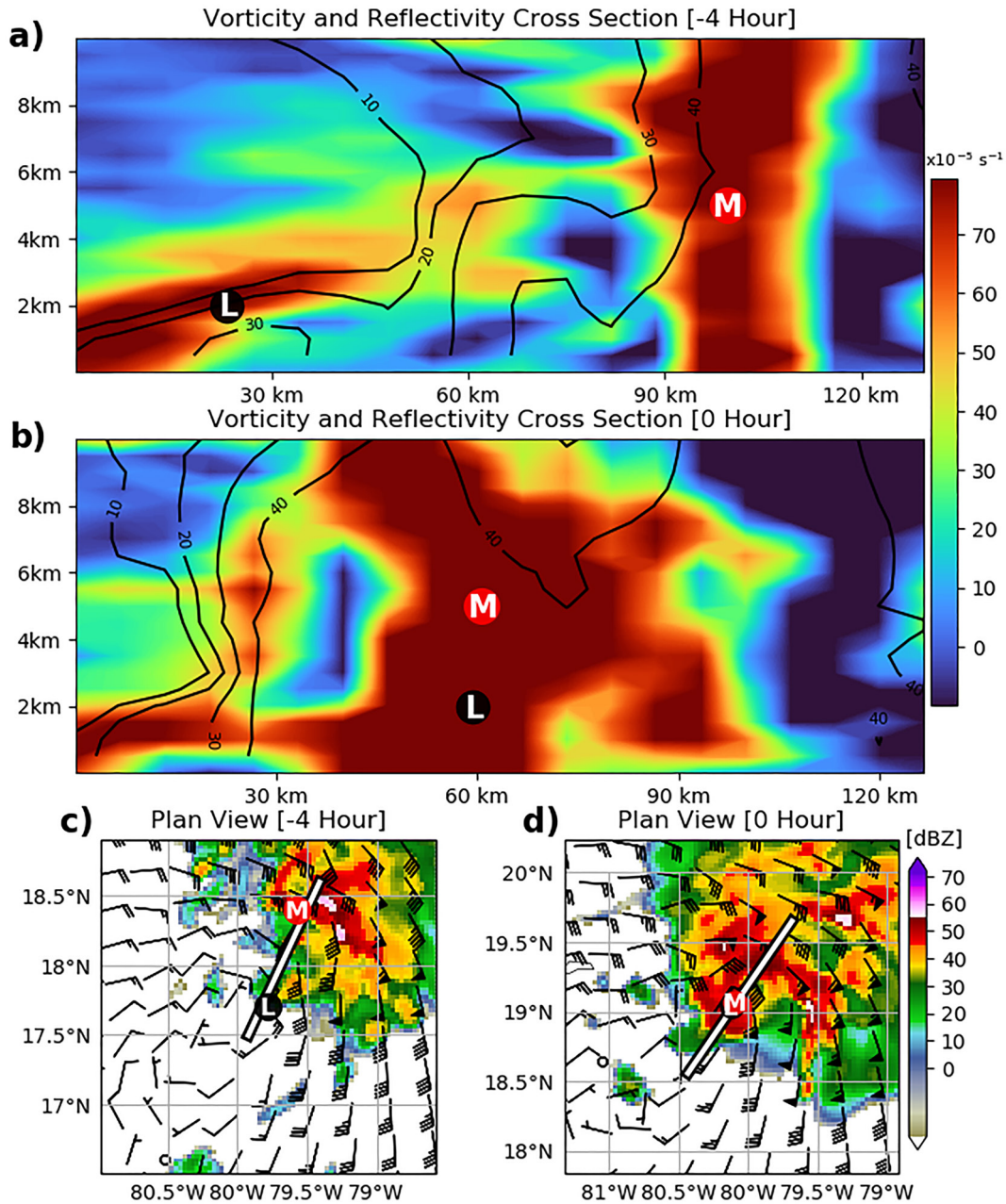

Figure 10. Relative vorticity (10^{-5} s^{-1}, color fill) cross section of Ida (2021) with respect to height and averaged across a line extending from the LLC to MLC (within 10 km) at −4 hr pre-alignment (top panel, a) and alignment (0 hr, b). Line contours indicate the average reflectivity (dBZ) along the cross section. Plan view plots of the cross sections (black and white line) at −4 hr pre-alignment (c) and alignment (0 hr, d) are shown with 2-km reflectivity (dBZ, color fill) and wind (kt, barbs). The "L" indicates the 2-km center and the "M" indicates the 5-km center in all four panels.

Figure 12a demonstrates this with the 2-km irrotational wind (blue line) increasing from ∼3–4 m/s at −6 hr to 5–7 m/s from −4 to 0 hr. To further determine the magnitude of the 2-km irrotational wind directed toward the MLC, the radial component is computed (purple line); and it increases from ∼2–3 m/s to 6–7 m/s during the 6-hr period preceding alignment. Although part of the increase in 2-km irrotational wind shown here is due to the migration of the LLC toward the MLC (Figures 11i and 11j), wherein the convergent irrotational flow is greater, the irrotational flow near the MLC also increased throughout this period (not shown). Therefore, at least some of the alignment can be attributed to advection. It is important to remember, however, that deep convective increases near the MLC are critical to this advection. This is demonstrated by the areal coverage (%) of deep convection

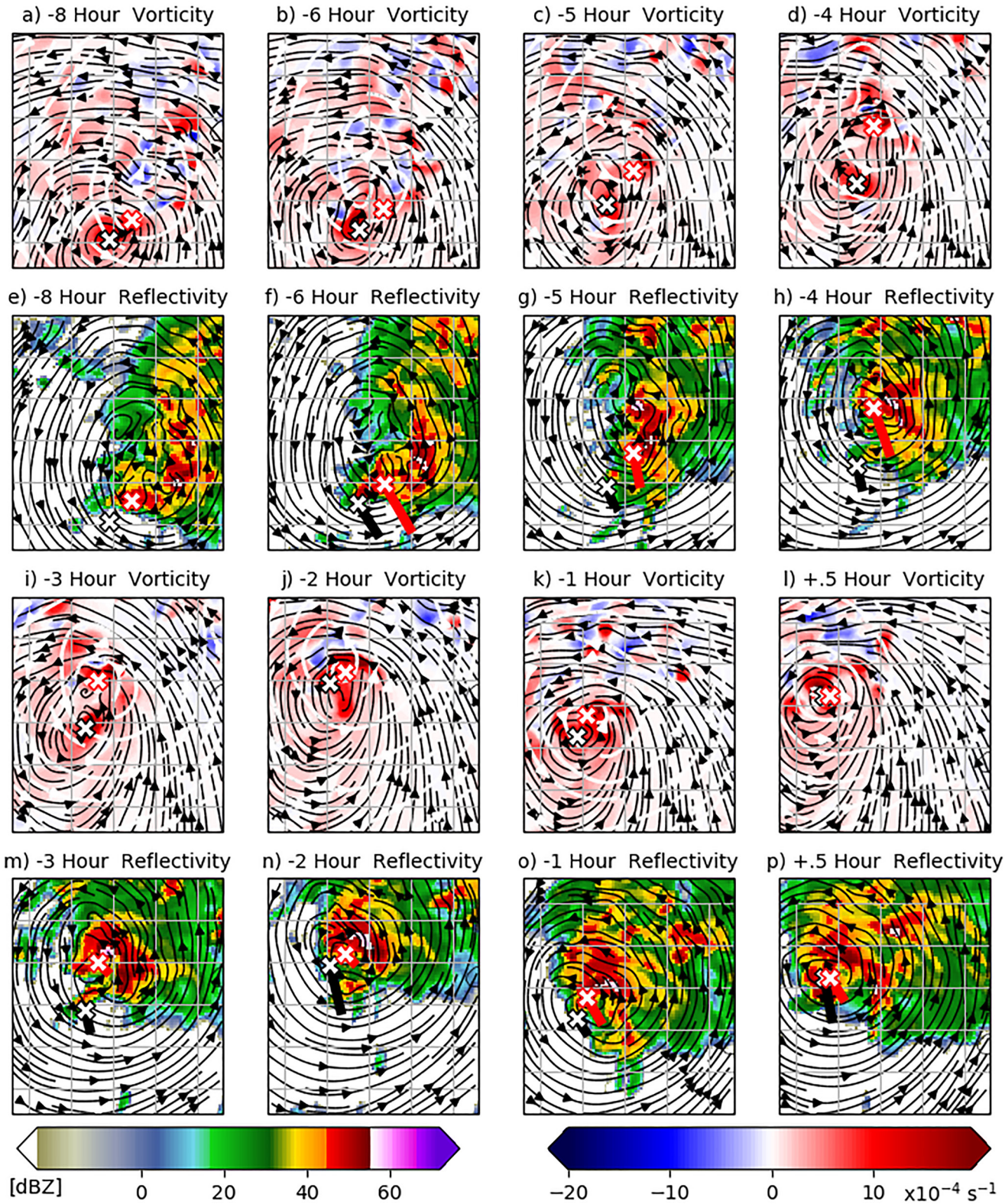

Figure 11. The top panels of each time subset show 2-km relative vorticity (color shading, $10^{-4}s^{-1}$), 2-km storm relative streamlines (black), and 5-km storm relative streamlines (white) at (a, b, c, d, i, j, k, and l) −8, −6, −5, −4, −3, −2, −1, +0.5 hr with respect to alignment time for Ida (2021). Each grid box (gray lines) represents 0.5° latitude and longitude. The black *X* with white fill (red *X* with white fill) indicates the 2-km (5-km) center and the trailing black (red) line indicates the center position change from the previous panel. The bottom panels show 5-km storm relative streamlines (black) and 2-km reflectivity (color shading, dBZ) at (e, f, g, h, m, n, o, and p) −8, −6, −5, −4, −3, −2, −1, +0.5 hr with respect to alignment time.

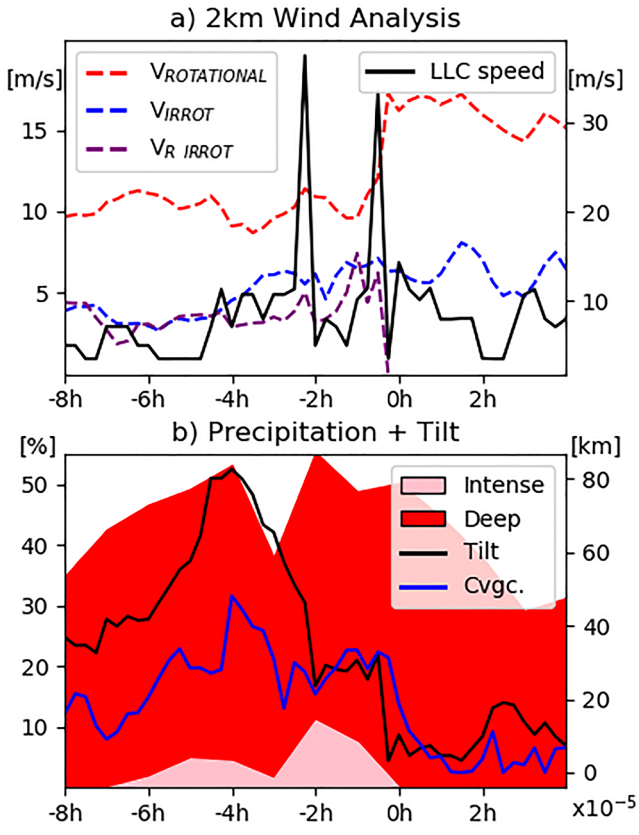

Figure 12. In panel (a), motion of the 2-km LLC (solid black, right *y*-axis) with respect to Ida's alignment time (0 hr). The 2-km rotational wind (dashed red, left *y*-axis) and irrotational wind (dashed blue, left *y*-axis) are averaged within 30 km of the 2-km center position. The radial component of the 2-km irrotational wind (averaged within 30 km of the 2-km center, positive values are inflow toward the MLC) is plotted by the purple dashed line (left *y*-axis). Panel (b) shows the coverage (%) of intense convection (pink shading, left *y*-axis) and deep convection (red shading, left *y*-axis) within 50 km of the MLC. 2-km convergence within 50 km of the MLC is shown by the blue line (right *y*-axis), and 2–5-km vortex tilt by the black line (right *y*-axis).

(red area) within 50 km of the MLC (Figure 12b), which increases from 35% at −8 hr to 50%–55% in the 2 hr preceding alignment. The areal coverage of intense convection (pink line) is defined by the convective pixels with a 40-dBZ echo top height >7 km, which represents the 99th percentile of 40-dBZ echo top heights for all simulations in this study. This 7-km threshold is approximately 1–2 km higher than what Cecil et al. (2002) found in oceanic and TC environments but is not surprising given the high reflectivity bias commonly noted within numerical models (Hazelton et al., 2021). The intense convection distribution increases from 0% at −8 hr to ∼5% by −4 hr, which also coincides with 2-km convergence (about the MLC) increasing from ∼20 ($\times 10^{-5}$ g kg^1 s^{-1}) to greater than 40 ($\times 10^{-5}$ g kg^1 s^{-1}). The coverage of intense convection peaks near 10% just prior to alignment at −2 hr. In summary, the irrotational component of the wind features a convergent flow at 2 km toward the centroid of deep convection that increases in intensity and areal coverage near the 5-km center.

Although the enhancement of irrotational wind undoubtedly plays a role, the rotational wind component has a 2–3 times greater magnitude than the irrotational wind throughout the pre-alignment period (Figure 12a, red line), as is commonly the case for vortical flow (Schecter & Menelaou, 2020). We also find that the 2 and 5-km rotational winds become enhanced on the eastern side (not shown) of the MLC as the deep convection increases and propagates northward, also indicated by the rotational wind at 2 km increasing from 10 to 15 m/s (Figure 12a). Finally, two distinct 2-km center jumps are apparent in Figure 12a (black line), one near −2 hr and one just before alignment. The first center jump is caused by the LLC accelerating toward the MLC (Figures 11i and 11j) and reformed vortex core due to the reshaped irrotational wind field (fostered by intense convection) described in the previous paragraph. The second center jump results in a tilt reduction from ∼30 km to less than 10 km (Figure 12a) and is likely an unphysical byproduct of the center finding algorithm. During this second jump, deep convection associated with the rapidly strengthening reformed vortex promotes the formation of vorticity beneath the MLC; and as the positive vorticity associated with the LLC that previously accelerated northward begins to mix and aggregate with this 2-km vorticity into one consolidated parent LLC (Figures 11k and 11l), a jump in the LLC occurs in the center finding algorithm.

3.5.2. Vorticity Budget

To more thoroughly explore the physical processes responsible for the progression from misalignment toward alignment in Ida, demonstrated by Figures 10 and 11, this section uses a storm-relative vorticity budget analysis (Alvey et al., 2020; X. Chen et al., 2018). Storm-relative vorticity budgets in Figure 13 are constructed with respect to the 2-km and 5-km centers to capture processes associated with both circulations prior to alignment. Figure 13a shows that the vorticity at −8 hr is maximized near 50×10^{-5} s^{-1} (white contours) below 3 km with respect to the 2-km center; however, values rapidly decrease with height to less than 10×10^{-5} s^{-1} above 7 km and are substantially less than the 30–40 $\times 10^{-5}$ s^{-1} (white contours) averaged around the 5-km center above 7 km (Figure 13b), a reflection of the vortex misalignment during this period. Vorticity near the 5-km center (Figure 13b) has slightly lower values (40×10^{-5} s^{-1}) in the lower troposphere; however, unlike the vertical profile in Figure 13a, vorticity associated with the robust MLC does not decrease significantly with height and in fact maximizes in the 5–8 km layer at later time periods (−6 to −4 hr). Although the stretching term initially has positive contributions near the 2-km center below ∼2 km (Figure 13c), during the −6 to −4 hr period values become predominantly negative and reflect a slight decrease in the overall low-level vorticity (and weaker LLC). This period also coincides with a misalignment increase from 40 to 80 km (Figure 12b), with deep convection also displaced farther from the LLC. On the other hand, the stretching term is much greater near the 5-km center (Figure 13d), as evident from positive

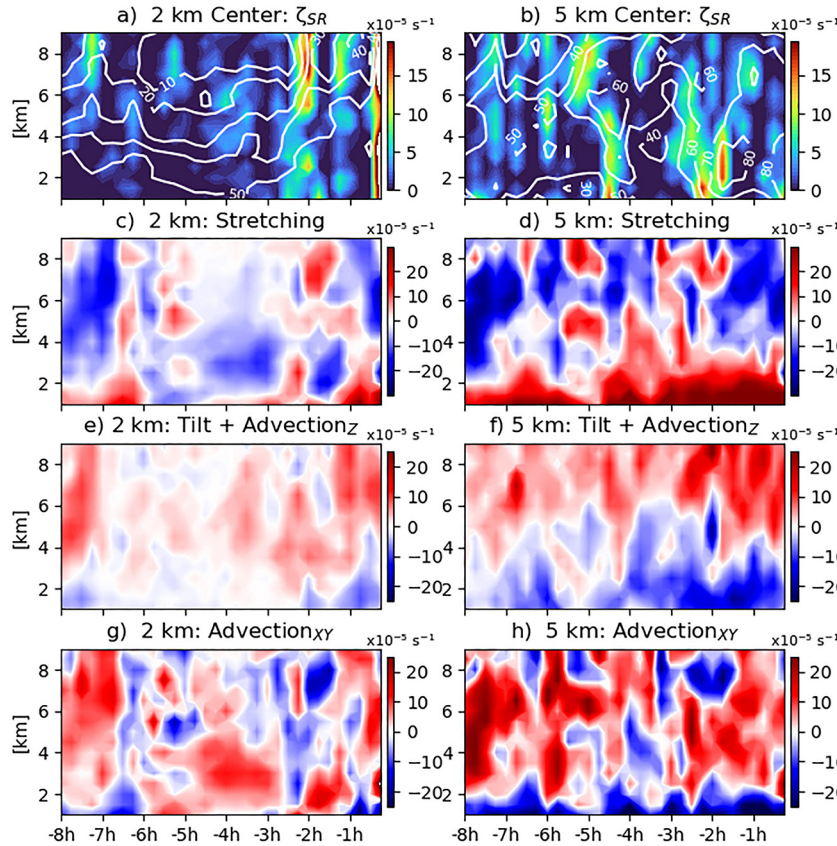

Figure 13. Storm-relative vorticity budget Hovmöllers for Ida with respect to alignment time and height. The vorticity is averaged within 40 km of the (a, c, e, and g) 2-km center and (b, d, f, h) 5-km center. Panels (a and b) show the vorticity change over 15-min (shading) and vorticity magnitude (white contour, 10^{-5} s^{-1}). Vorticity budget terms (15-min accumulation) are shown in panels as follows: c and d (stretching term), e and f (tilting plus vertical advection term), g and h (horizontal advection term).

values exceeding 10–20 × 10^{-5} s^{-1} below 2 km, and a reflection of the significantly greater distribution of deep convection near the MLC (Figure 12b).

Around −5 to −4 hr the vorticity near the MLC rapidly increases by >10 × 10^{-5} s^{-1} to ∼65 × 10^{-5} s^{-1} in the middle troposphere (Figure 13b) and to ∼45 × 10^{-5} s^{-1} in the lower troposphere, and is likely the result of a compact vortex core reformation from 1 to 6 km (also evident from the MLC "jump" in Figures 11g and 11h). We speculate these increases in vorticity are connected to deep CBs given the large increases in the stretching term in the 1–6-km layer (Figure 13d) and tilting + vertical advection terms (Figure 13f) above 4 km. Following this vortex core reformation (−4 to −2.5 hr), the vorticity with respect to the 2-km center (Figure 13a) gradually increases throughout the troposphere, a period during which the LLC also begins to accelerate toward the newly reformed vortex (Figures 11i and 11j).

At −2 hr the vorticity with respect to the 2-km center (Figure 13a) rapidly increases throughout the troposphere (most significantly above 5 km, ∼20 × 10^{-5} s^{-1} increase) and reflects the acceleration of the LLC toward the MLC (misalignment decreases to ∼25 km) shown in Figures 11j, 11n, and 12a. Positive contributions from the stretching term (Figure 13c) and the tilting and vertical advection terms (2–6 km, Figure 13e) also increased during this period as deep convection associated with the MLC is now also located near the LLC. Vorticity with respect to the 5-km center (Figure 13b) also rapidly increases in the 1–6-km layer (most significantly below 4 km) between −3 and −1.5 hr, attributed to the 2-km center accelerating toward the 5-km center; this is also reflected by the increases in horizontal vorticity advection below 6 km from −3 to 0 hr (Figure 13h). The stretching term, unsurprisingly, has positive values in the lower troposphere below 4 km throughout the period (Figure 13d). An increase in the 1–3 km-layer between −3 and 0 hr, however, is notable because it also coincides with a slight

uptick in convective coverage (Figure 12b) and migration of the LLC toward the MLC (Figures 11i and 11j). The tilting and vertical advection terms are predominantly negative below 4 km and positive above 5–6 km (Figure 13f), a reflection of the predominantly convective regime near the MLC. This evolution of vorticity core reformation followed by advective confluence of the LLC toward the reformed vortex has features of multiple alignment pathways. Nguyen and Molinari (2015) and X. Chen et al. (2018) described the reformation pathway, whereas Schecter and Menelaou (2020) used idealized simulations in a shear-free environment to identify alignment through advection of the low-level vortex toward the mid-level vortex (facilitated by convectively driven inflow near the midlevel vortex), potentially accompanied by a mixing of diabatically generated vorticity. Although we have demonstrated the importance of increases in the areal coverage and intensity of deep convection for vortex reformation (and alignment), Section 3.5.4 will investigate hypothesized causes of the increases in persistent, deep convection.

3.5.3. Causes of Increases in Deep Convection That Result in Alignment

Sections 3.4.1 and 3.4.2 (Figures 5–7) have already shown the link between mid-tropospheric RH increasing in the downshear quadrants 12–24 hr before alignment and increases in deep convection. This section will test additional hypotheses that link beneficial contributions from physical processes that enhance instability and lead to deep convection. In order to better demonstrate the detailed thermodynamic processes associated with increases in deep convection and tilt reduction, Figure 14 examines the vortex-scale evolution of instability during Ida's pre-alignment period. At −10 hr the misalignment between the MLC and LLC is about 50 km (Figure 14a). Although some intense convection (defined as in Figure 12) is concentrated near the LLC, a large area of convective inhibition (CIN) is preventing precipitation in the southwestern quadrant. Meanwhile, a new large region of intense convection has developed just south of Jamaica. Overall, convective available potential energy (CAPE) is 1,000–2000 J/kg within the inflow region (from the southeast). By −4 hr (Figure 14b) the LLC and MLC remain misaligned, however, the MLC is now associated with a reforming vortex core near the area of intense convection toward the northeast (also shown in Figures 10a, 10c,, and 11h). CAPE values have increased within the inflow region to 2,000–2,500 J/kg by −4 hr and even more so by −2 hr (Figures 14b and 14c), helping to sustain intense convection near the reformed vortex. It has not yet been shown, however, what is causing the instability increases: Are near-surface fluxes increasing or is the mid-upper troposphere cooling (due to cooling beneath the mid-level potential vorticity anomaly; Raymond et al., 2014)?

We hypothesize that the increasingly confluent irrotational flow directed toward the convection associated with the reforming vortex core (near the MLC position) during this period (Figure 12a) acts as a convergent source for favorable boundary layer thermodynamics, thereby increasing the instability and maintenance of persistent convection. A subjectively chosen section of the inflow region is denoted by the blue boxes (Figures 14d and 14e) and can also be visualized with near-surface streamlines in Figure 14g. Figure 14d shows that the surface equivalent potential temperature (θ_e) tends to maximize in regions with the greatest instability at −10 hr. The most prominent surface latent heat fluxes, however, are located in the precipitation cooled region north of the MLC from −10 to −4 hr. By −4 hr the surface θ_e values increase significantly from 357–359 K to >360 K upstream of the MLC and the most intense convection in the inflow region (Figure 14e, also highlighted by the blue box). A small area of surface latent heat fluxes >350 W/m^2 extends into the inflow by −4 hr (Figure 14e), likely a result of ∼5–10 kt increases in tangential wind (Figures 14d and 14e) and a slight increase in SSTs locally (∼0.2–0.5°C, not shown). Figure 14i demonstrates that the increases in instability within the inflow region are primarily driven by increases in boundary layer θ_e. Most notably, the areal averaged dewpoint temperature increases from −10 to −4 hr below 600 hPa, which results in the most attributable CAPE increases (pink shading). By −2 hr the MLC and LLC are nearly aligned with intense convection continuing to persist in the eastern quadrant along the axis of greatest instability, now >2,500 J/kg (Figure 14c). In addition to the stronger surface wind helping to increase the boundary layer moisture and instability, we'll demonstrate next that outflow boundaries and changes in downdrafts may have also played a role in sustaining convection.

The initial downtilt increase in intense convection near −10 hr (Figure 14a) generates cold pools, which are evident as depressed near-surface θ_e values <350 K downstream (Figure 14d) of vertical velocity <−0.5 m/s indicative of downdrafts (Figure 14d, white contours). This helps to establish a quasi-stationary (storm-relative frame of reference) outflow boundary, also demonstrated by the east-southeasterly near-surface streamlines in Figure 14g converging with northeasterly winds near the θ_e gradient (Figure 14a). We speculate that this boundary may have helped amplify the upstream reservoir of high θ_e air (θ_e ridge, Scofield, 1990) through moisture

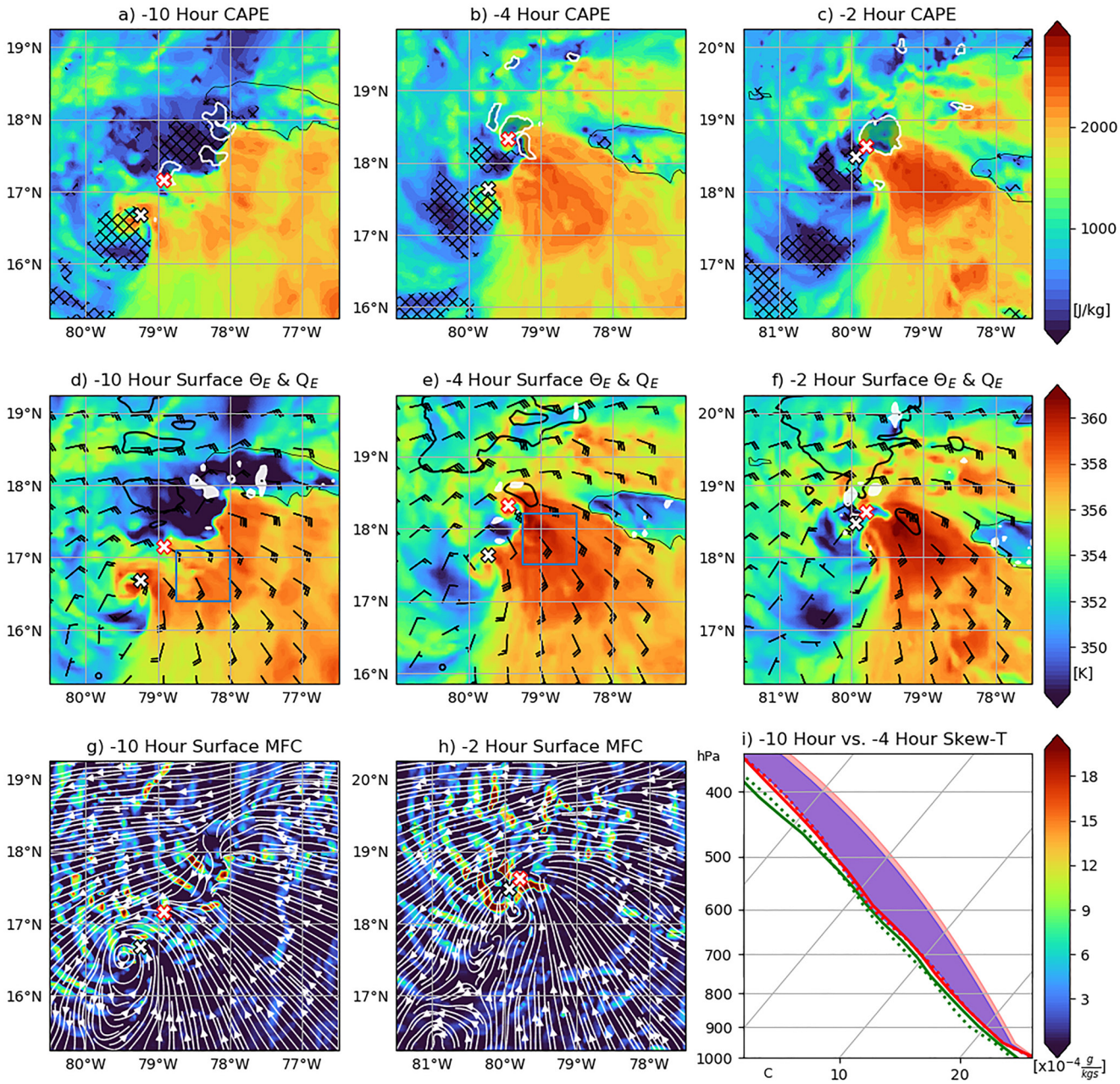

Figure 14. Surface-based convective available potential energy (CAPE in J/kg, color-shading) for Ida (2021) at (a) −10, (b) −4, and (c) −2 hr pre-alignment. Black hatched areas indicate convective inhibition (CIN) greater than 20 J/kg. The black *X* (white fill) denotes the 2-km center and the red *X* (white fill) denotes the 5-km center. Light black (transparent) shading outlined by white lines indicates the areal extent of intense convection. Surface θ_e (color shading), latent heat flux (black line contour, >350 W/m^2), and 1-km vertical velocity (white contour and shading, <−0.5 m/s) at (d) −10 hr, (e) −4 hr, and (f) −2 hr. Surface moisture flux convergence (MFC, $\times 10^{-4}$ g kg^{-1}s^{-1}, color shading) and streamlines at (g) −10 hr and (h) −2 hr. The blue boxes in (d and e) denote the areal averaged Skew-T profiles within the inflow region shown in panel (i) with −10-hr temperature (red dashed), −10-hr dewpoint (green dashed), −10-hr CAPE (purple fill), −4-hr temperature (red solid), −4-hr dewpoint (green solid), and −4-hr CAPE (purple + pink).

pooling (Fuglestvedt & Haerter, 2020), which is also reflected in the localized moisture flux convergence (MFC) maxima (Figure 14g). The broad low-level vortex structure and storm-relative streamlines (Figure 14g) also indicate that most of this downstream air in Ida associated with the cold pools likely did not unfavorably re-circulate back into the convective inflow region and/or was also able to recover via surface fluxes. In the ensuing 6 hr, the areal extent of downdrafts decreases, which may have also contributed to the previously discussed boundary layer thermodynamic recovery north and west of the MLC (left of shear). By −2 hr, MFC remains maximized near the

outflow boundaries and the region of most intense convection. Although many studies have shown that downdraft driven cold pools are often unfavorable for TC intensification (Alland et al., 2021a), this analysis highlights the nuanced nature of early stage TC development wherein downdrafts may not always deter TC intensification if they are weaker and/or have a smaller areal coverage. In fact, a previous idealized modeling study of TC genesis by Davis (2015) highlighted the instrumental role of downdraft-driven cold pools in initiating strong updrafts and contributing to convective organization. The magnitude and effects of downdraft ventilation may perhaps also be dependent upon other conditions like mid-tropospheric moisture, boundary layer recovery processes, and low-level vortex structure. In summary, we hypothesize that the reformed vorticity core in Ida benefits from a positive feedback: The thermodynamically beneficial effects of the cold pool that initially forms downtilt (e.g., moisture pooling and convergence) promote upstream convection, which further increases inflow strength, amplifies instability, and enhances moisture convergence to help convection persist, a critical characteristic for vortex reformation and diabatically induced advection that contributes to alignment.

3.6. Causes of Alignment Differences Between Elsa and Ida

This section expands upon analyses from Section 3.4 to explore in more detail why Elsa was unable to achieve sustained alignment (Figure 2i). Figure 5 demonstrated that the mid-tropospheric humidity in Elsa left of shear was comparable if not greater than Ida, however, much drier air was located in the right of shear quadrants. As in Figure 14, we plot the CAPE for Elsa in Figures 15a–15c to investigate the potential effects of the dry air in more detail. At −5 hr (Figure 15a) Elsa is misaligned by more than 80 km with areas of disorganized intense convection displaced away from the centers and 1,000–1,500 J/kg CAPE with locally greater maxima near and south of the centers. Although the centers become nearly aligned at 0 hr, an area of low CAPE (<500 J/kg) and high CIN north of the MLC propagates from the northeast quadrant to the southwest quadrants, resulting in a narrowing of the instability axis. The low CAPE region largely coincides with low, unfavorable near-surface Θ_E air (<348 K, Figure 15d) propagating cyclonically around Elsa in a much more expansive pattern than Ida (Figures 14d–14f). This larger, more expansive unfavorable thermodynamic region in Elsa is downstream of a significantly greater coverage of downdrafts (Figure 15d, white contours), which given the lower mid-tropospheric RH, indicates a high likelihood of downdraft ventilation. By +5 hr (Figure 15c) the thermodynamic favorability surrounding Elsa further deteriorates with low CAPE and high CIN values nearly surrounding the TC centers. These unfavorable thermodynamics coincide with a lack of persistent convection in spite of a greater areal coverage of high surface latent heat fluxes (>350 W/m^2, Figure 15d) near the centers than in Ida (Figures 14b and 14c). To further demonstrate the impact of the potential dry air intrusion in Elsa, the Skew-T diagram (Figure 15e) shows that significantly drier air extends through the troposphere than in Ida, most prominent above 550 hPa. Although the lower tropospheric temperatures between Ida and Elsa are similar, the lower moisture values in Elsa result in a large reduction in CAPE. In contrast to Ida, Elsa demonstrates how convection near/within regions of dry mid-tropospheric air, can result in irrecoverable boundary layer conditions, a result also found by other studies (e.g., Alland et al., 2021a, 2021b; B. Tang & Emanuel, 2010, 2012).

One final ingredient that has yet to be explored thoroughly, the VWS, is demonstrated using a hodograph in Figure 15f. The large scale (0–500-km) VWS in both Elsa and Ida has fairly comparable hodograph shapes and magnitudes throughout the troposphere (Figure 15f, subpanel). Because weak TCs with misaligned vortices can result in local, vortex-scale variations in VWS, such as curved hodographs that enhance streamwise horizontal vorticity (Hogsett & Stewart, 2014), local VWS is also calculated over the blue box in Figure 14e and black boxes shown in Figure 15a. Elsa (solid black line hodograph, Figure 15f) has a disorganized local shear pattern near the LLC and MLC with some slight counterclockwise curvature in periodic segments but generally a straight line hodograph pattern in the mid-upper troposphere. On the contrary, the shear profile in Elsa near the most intense, persistent convection (Figure 15a, lower right black box near 23°N 82°W), features a much more favorable configuration for organized deep convection with counter-clockwise curvature of the winds (solid green, blue, purple lines) with increasing height throughout the troposphere. Ida (dashed line hodograph) similarly exhibits a localized shear profile near the most persistent deep convective region with strong counter-clockwise turning of the winds with increasing height. We hypothesize that despite the similar local shear profiles near convection, the location of the convection downshear right in Elsa was unfavorably located nearer to dry mid-tropospheric air (Figures 5b–5d), which resulted in the more unfavorable boundary layer thermodynamics previously shown and were detrimental factors preventing reformation and/or sustained alignment in this circumstance.

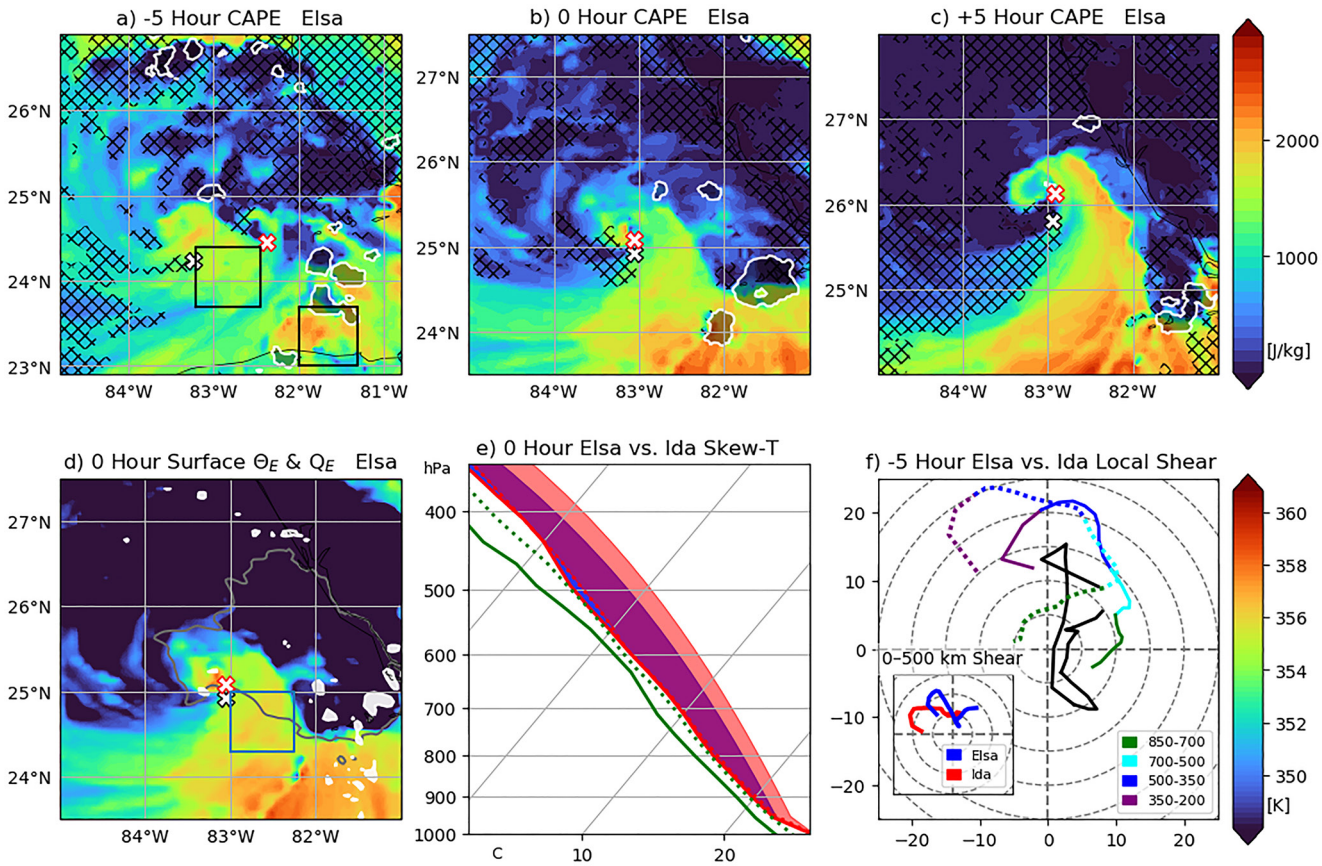

Figure 15. Surface-based convective available potential energy (CAPE in J/kg, color-shading) for Elsa (2021) at (a) −5, (b) 0, and (c) +5 hr with respect to attempted alignment. Black hatched areas indicate convective inhibition (CIN) greater than 20 J/kg. The black *X* (white fill) denotes the 2-km center and the red *X* (white fill) denotes the 5-km center. Light black (transparent) shading outlined by white lines indicates the areal extent of intense convection. Surface Θ_E (color shading), latent heat flux (dark gray line contour, >350 W/m^2), and 1 km vertical velocity (white contour and shading, <0.5 m/s) at (d) 0 hr. The blue box in (d) denotes the areal averaged Skew-T profile shown in panel (f) with 0-hr temperature (red solid), dewpoint (green solid), and CAPE (purple fill) compared to Ida's −4-hr temperature (red dashed), dewpoint (green dashed), and CAPE (purple + salmon). Panel (g) shows the −5-hr local shear hodograph [m/s] calculated within the black box near 23°N 82°W in (a) for Elsa (and blue box for Ida in Figure 14e) at 850–700 hPa in solid (dashed) green, 700–500 hPa in solid (dashed) cyan, 500–350 hPa in solid (dashed) blue, and 350–200 hPa in solid (dashed) purple. The black line indicates the 850–200-hPa wind profile averaged within the black box near 24°N 83°W in (a). The subpanel shows a hodograph of the 850–200-hPa wind averaged within 0–500 km of the LLC for Elsa (blue) and Ida (red).

4. Summary

This study simulates five weak, moderately sheared TCs (Elsa, Ida, Isaias, Nicholas, Sally) from 2020 to 2021 Atlantic Basin hurricane season using the Hurricane Analysis Forecast System (HAFS). Model runs are compared with radar and airborne observations to identify the model cycles that most accurately portray the observed tilt evolution. All but one simulation, Elsa (2021), undergo a successful transition from misalignment toward alignment. While there are differences from the model and observations in the magnitudes of both intensity and tilt, qualitatively the simulations selected represent the observed evolution sufficiently. While some of the cases like Ida (2021) exhibit qualities of vortex reformation and/or rapid diabatically induced advection processes, others like Sally (2020) have smaller initial tilts (and stronger initial vortices) with a precessional progression toward alignment.

Initially, the most significant increases in mid-tropospheric humidity pre-alignment are observed in the DSL quadrants in the 4 successful simulations (Isaias, Sally, Ida, Nicholas). And despite alignment at 0 hr, the highest mid-tropospheric RH values remain confined DSL, a result similar to Alvey et al. (2020). The USL RH values increase most substantially following alignment as this vortex configuration provides a more efficient pathway for rapid increases in precipitation and moisture advection from the favorable DSL quadrant. The failed alignment simulation, Elsa, has comparably high mid-tropospheric RH values left of shear, however, much drier air is

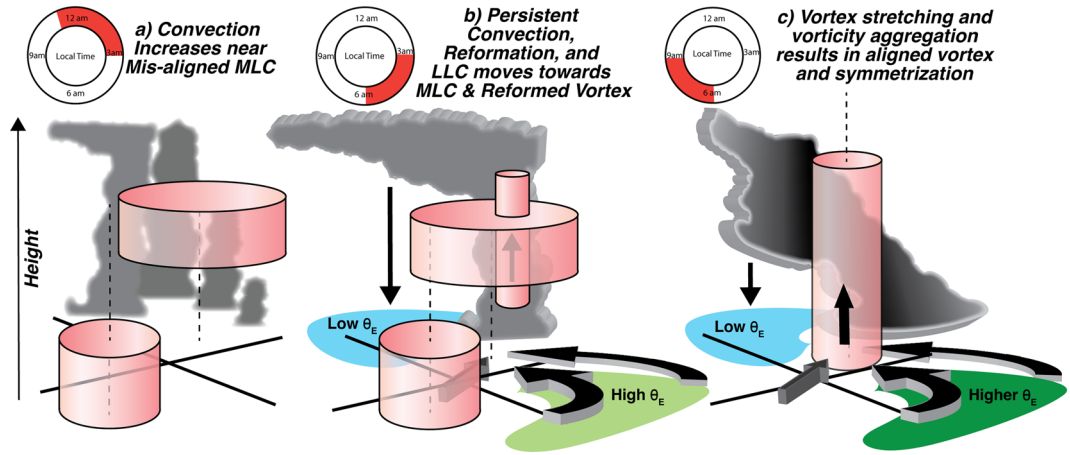

Figure 16. Schematic demonstrating the vortex-scale processes responsible for a rapid evolvement from misalignment to alignment. Panel (a) shows the low-level vortex displaced from the mid-level vortex with convection increasing near the MLC (indicated by the clouds). The increasing convection near the MLC occurs during the overnight to early morning hours of 11 p.m. to 3 a.m. (upper left), which also aligns with the diurnal maximum in TC convection (Ditchek, Molinari, et al., 2019; Dunion et al., 2014). At 3–6 a.m. local time (panel b), the boundaries between lower θ_E air from downdrafts (light blue shading) and warm, unstable air (higher θ_E air, light green shading) collide and initiate more intense, persistent convection. A new, compact low-mid level vorticity core forms near the convection and induces a low-level confluent inflow that brings more warm, moist air (light green shading) toward the new center fueling additional convection. The LLC rapidly migrates towards the reformed core during this time period.

located near/within the inner core right of shear, which likely detrimentally results in downdraft ventilation. In the successful alignment simulations, significant increases in stratiform precipitation were also found DSL in the 12 hr preceding alignment, which correlates to the observed humidity increases. An increase in stratiform precipitation USL near alignment precedes the humidification in that quadrant by 6–12 hr. This result indicates the important role that stratiform plays in creating a humid, more favorable environment for sustained precipitation symmetry (Alvey et al., 2020). On the other hand, the areal coverage of deep convection does not propagate as far USL. Vertical velocity, also used a proxy for convection, shows the most marked increase in coverage and intensity DSL in the 3–6 hr pre-alignment. By contrast, the simulation with a failed alignment not only has a smaller areal coverage and less persistent convection but precipitation also remains confined DSL farther from the center.

Ida (2021) is selected as a representative case to show the vortex-scale processes and the related precipitation properties responsible for a rapid evolvement from misalignment to alignment in just 6 hr. A schematic of these processes in Figure 16 shows that an increase in both areal coverage and intensity of deep convection downtilt near the MLC first occurs during the early morning hours (local time). Similar to the (downshear) vortex reformation in Nguyen and Molinari (2015) and X. Chen et al. (2018), an evolution is then observed in which a compact vorticity core (Figure 16b) reforms within the broader mid-level circulation. Whereas those studies found that reformation abruptly led to the formation of a new LLC beneath the MLC, the reformation in Ida does not immediately result in the formation of a new, closed LLC beneath the MLC. Rather, alignment does not complete until after the vertical mass flux associated with the deep convection (that reforms the vorticity core) causes the low-level confluence to direct the LLC inward resulting in tilt reduction and eventual alignment (Figure 16b), a similar evolution to Schecter and Menelaou (2020). The persistence of convection downtilt is hypothesized to ultimately help reshape the lower troposphere irrotational velocity field toward the MLC (reformed vortex). A vorticity budget also shows that the stretching term is initially much greater near the 5-km center, reflecting the significantly greater distribution of deep convection near the MLC and its importance to the alignment process (Raymond & Sessions, 2007; Raymond et al., 2014; Rogers et al., 2020). The MLC jump is shown to be associated with a vorticity core reformation as the stretching, tilting, and vertical advection terms provide positive vorticity tendencies through the lower-middle troposphere. Vorticity near the 2-km center only increases in the middle-upper troposphere after it advects toward the MLC where convection is focused.

In trying to determine the mechanisms responsible for persistent, intense convection downtilt near the MLC (that results in alignment) in Ida, we hypothesize that the increasingly confluent irrotational flow directed toward

the MLC during this period increases surface fluxes and acts as a convergent source for favorable boundary layer thermodynamics (Figure 16c), thereby increasing the instability and maintenance of persistent convection. Additionally, a positive feedback develops where outflow boundaries associated with cold pools downtilt provide indirect thermodynamic benefits (e.g., moisture pooling and convergence) to promote upstream convection maintenance, which further increases inflow strength, amplifies instability, and enhances moisture convergence to help convection persist. On the contrary, proximity of dry air near deep convection in Elsa likely results in entrainment, downdraft ventilation, and more expansive, unfavorable cold pools than Ida. Localized vertical wind shear profiles with curved counter-clockwise hodographs are also speculated to play a role in the persistence of convection. Finally, contributions from the diurnal cycle in successful alignment simulations show that convection preferentially increases near the center during the early morning hours and, on average, corresponds with tilt reduction. This indicates the potential usefulness of local time as a predictor of tilt evolution and intensity change.

This study highlights the complicated and rapid vortex-scale evolution that can occur in weak, misaligned TCs. The addition of more cases and idealized experiments would be beneficial toward future work to help address unanswered questions like whether or not alignment would have occurred/persisted without the diabatically generated advection of the LLC toward the reformed vortex. More comprehensive observational data (Zawislak et al., 2022) are also needed to provide better contextualization of individual cases and progress toward identifying unique characteristics (environmental and vortex-scale) associated with different alignment pathways.

Data Availability Statement

The necessary code to compile figures in this manuscript are readily available in pre-existing Python packages (e.g., Python Software Foundation, https://www.python.org/). Because of the large file sizes of simulations, this data will be provided only upon request through a remote-ftp.

Acknowledgments
The authors would like to thank Michael Fischer and three anonymous reviewers for providing valuable feedback on the manuscript. The authors would also like to thank Cayman Islands National Weather Service for providing ground radar data. The authors would further like to thank William Ramstrom for providing assistance with HAFS high resolution output. This research is supported by NOAA grant NA19OAR0220187.

References

Alland, J. J., Tang, B. H., Corbosiero, K. L., & Bryan, G. H. (2021a). Combined effects of midlevel dry air and vertical wind shear on tropical cyclone development. Part I: Downdraft ventilation. *Journal of the Atmospheric Sciences*, *78*(3), 763–782. https://doi.org/10.1175/jas-d-20-0054.1

Alland, J. J., Tang, B. H., Corbosiero, K. L., & Bryan, G. H. (2021b). Combined effects of midlevel dry air and vertical wind shear on tropical cyclone development. Part II: Radial ventilation. *Journal of the Atmospheric Sciences*, *78*(3), 783–796. https://doi.org/10.1175/jas-d-20-0055.1

Alvey, G. R., III, Fischer, M., Reasor, P., Zawislak, J., & Rogers, R. (2022). Observed processes underlying the favorable vortex repositioning early in the development of Hurricane Dorian (2019). *Monthly Weather Review*, *150*(1), 193–213. https://doi.org/10.1175/mwr-d-21-0069.1

Alvey, G. R., III, Zawislak, J., & Zipser, E. (2015). Precipitation properties observed during tropical cyclone intensity change. *Monthly Weather Review*, *143*(11), 4476–4492. https://doi.org/10.1175/mwr-d-15-0065.1

Alvey, G. R., III, Zipser, E., & Zawislak, J. (2020). How does Hurricane Edouard (2014) evolve toward symmetry before rapid intensification? A high-resolution ensemble study. *Journal of the Atmospheric Sciences*, *77*(4), 1329–1351. https://doi.org/10.1175/jas-d-18-0355.1

Bell, M. M., Dixon, M., Javornik, B., Lee, W., Melli, B., DeHart, J., & Cha, T. (2020). nsf-lrose/lrose-cyclone: Lrose-cyclone release 20200110 (lrose-cyclone-20200110) [Dataset]. Zenodo. https://doi.org/10.5281/zenodo.3604387

Bell, M. M., & Montgomery, M. T. (2019). Mesoscale processes during the genesis of Hurricane Karl (2010). *Journal of the Atmospheric Sciences*, *76*(8), 2235–2255. https://doi.org/10.1175/jas-d-18-0161.1

Bender, M. A., Marchok, T. P., Sampson, C. R., Knaff, J. A., & Morin, M. J. (2017). Impact of storm size on prediction of storm track and intensity using the 2016 operational GFDL hurricane model. *Weather and Forecasting*, *32*(4), 1491–1508. https://doi.org/10.1175/waf-d-16-0220.1

Beven, J. L., II, Hagen, A., & Berg, R. (2022). Tropical cyclone report: Hurricane Ida (26 August–1 September 2021). *NHC Technical Report AL092021* (p. 163). Retrieved from https://www.nhc.noaa.gov/data/tcr/AL092021_Ida.pdf

Boehm, A. M., & Bell, M. M. (2021). Retrieved thermodynamic structure of Hurricane Rita (2005) from airborne multi–Doppler radar data. *Journal of the Atmospheric Sciences*, *78*(5), 1583–1605. https://doi.org/10.1175/jas-d-20-0195.1

Brown, D. (2020). *AL19 forecast advisory* (Vol. 12). National Hurricane Center. Retrieved from https://www.nhc.noaa.gov/archive/2020/al19/al192020.discus.012.shtml?

Cangialosi, J. P., Blake, E., DeMaria, M., Penny, A., Latto, A., Rappaport, E., & Tallapragada, V. (2020). Recent progress in tropical cyclone intensity forecasting at the National Hurricane Center. *Weather and Forecasting*, *35*(5), 1913–1922. https://doi.org/10.1175/waf-d-20-0059.1

Cecil, D. J., Zipser, E. J., & Nesbitt, S. W. (2002). Reflectivity, ice scattering, and lightning characteristics of hurricane eyewalls and rainbands. Part I: Quantitative description. *Monthly Weather Review*, *130*(4), 769–784. https://doi.org/10.1175/1520-0493(2002)130<0769:risalc>2.0.co;2

Chen, H., & Gopalakrishnan, S. G. (2015). A study on the asymmetric rapid intensification of Hurricane Earl (2010) using the HWRF system. *Journal of the Atmospheric Sciences*, *72*(2), 531–550. https://doi.org/10.1175/jas-d-14-0097.1

Chen, J.-H., & Lin, S.-J. (2013). Seasonal predictions of tropical cyclones using a 25–km–resolution general circulation model. *Journal of Climate*, *26*(2), 380–398. https://doi.org/10.1175/jcli-d-12-00061.1

Chen, S. S., Knaff, J. A., & Marks, F. D., Jr. (2006). Effects of vertical wind shear and storm motion on tropical cyclone rainfall asymmetries deduced from TRMM. *Monthly Weather Review*, *134*(11), 3190–3208. https://doi.org/10.1175/mwr3245.1

Chen, X., Wang, Y., Fang, J., & Xue, M. (2018). A numerical study on rapid intensification of Typhoon Vicente (2012) in the South China Sea. Part II: Roles of inner-core processes. *Journal of the Atmospheric Sciences*, *75*(1), 235–255. https://doi.org/10.1175/jas-d-17-0129.1

Chen, X., Zhang, J. A., & Marks, F. D. (2019). A thermodynamic pathway leading to rapid intensification of tropical cyclones in shear. *Geophysical Research Letters*, *46*(15), 9241–9251. https://doi.org/10.1029/2019gl083667

Corbosiero, K. L., & Molinari, J. (2002). The effects of vertical wind shear on the distribution of convection in tropical cyclones. *Monthly Weather Review*, *130*(8), 2110–2123. https://doi.org/10.1175/1520-0493(2002)130<2110:teovws>2.0.co;2

Davis, C. A. (2015). The formation of moist vortices and tropical cyclones in idealized simulations. *Journal of the Atmospheric Sciences*, *72*(9), 3499–3516.

DeMaria, M. (1996). The effect of vertical shear on tropical cyclone intensity change. *Journal of the Atmospheric Sciences*, *53*(14), 2076–2088. https://doi.org/10.1175/1520-0469(1996)053<2076:teovso>2.0.co;2

Ditchek, S. D., Corbosiero, K. L., Fovell, R. G., & Molinari, J. (2019). Electrically active tropical cyclone diurnal pulses in the Atlantic basin. *Monthly Weather Review*, *147*(10), 3595–3607. https://doi.org/10.1175/mwr-d-19-0129.1

Ditchek, S. D., Molinari, J., Corbosiero, K. L., & Fovell, R. G. (2019). An objective climatology of tropical cyclone diurnal pulses in the Atlantic basin. *Monthly Weather Review*, *147*(2), 591–605. https://doi.org/10.1175/mwr-d-18-0368.1

Dong, J., Liu, B., Zhang, Z., Wang, W., Mehra, A., Hazelton, A., et al. (2020). The evaluation of real-time Hurricane Analysis and Forecast System (HAFS) Stand-Alone Regional (SAR) model performance for the 2019 Atlantic hurricane season. *Atmosphere*, *11*(6), 617. https://doi.org/10.3390/atmos11060617

Dunion, J. P., Thorncroft, C. D., & Nolan, D. S. (2019). Tropical cyclone diurnal cycle signals in a hurricane nature run. *Monthly Weather Review*, *147*(1), 363–388. https://doi.org/10.1175/mwr-d-18-0130.1

Dunion, J. P., Thorncroft, C. D., & Velden, C. S. (2014). The tropical cyclone diurnal cycle of mature hurricanes. *Monthly Weather Review*, *142*(10), 3900–3919. https://doi.org/10.1175/mwr-d-13-00191.1

Finocchio, P. M., Majumdar, S. J., Nolan, D. S., & Iskandarani, M. (2016). Idealized tropical cyclone responses to the height and depth of environmental vertical wind shear. *Monthly Weather Review*, *144*(6), 2155–2175. https://doi.org/10.1175/mwr-d-15-0320.1

Fischer, M. S., Reasor, P. D., Rogers, R. F., & Gamache, J. F. (2022). An analysis of tropical cyclone vortex and convective characteristics in relation to storm intensity using a novel airborne Doppler radar database. *Monthly Weather Review*, *150*(9), 2255–2278. (published online ahead of print 2022). https://doi.org/10.1175/mwr-d-21-0223.1

Fischer, M. S., Tang, B. H., & Corbosiero, K. L. (2019). A climatological analysis of tropical cyclone rapid intensification in environments of upper-tropospheric troughs. *Monthly Weather Review*, *147*(10), 3693–3719. https://doi.org/10.1175/mwr-d-19-0013.1

Fischer, M. S., Tang, B. H., Corbosiero, K. L., & Rozoff, C. M. (2018). Normalized convective characteristics of tropical cyclone rapid intensification events in the North Atlantic and eastern North Pacific. *Monthly Weather Review*, *146*(4), 1133–1155. https://doi.org/10.1175/mwr-d-17-0239.1

Frank, W. M., & Ritchie, E. A. (1999). Effects of environmental flow upon tropical cyclone structure. *Monthly Weather Review*, *127*(9), 2044–2061. https://doi.org/10.1175/1520-0493(1999)127<2044:eoefut>2.0.co;2

Frank, W. M., & Ritchie, E. A. (2001). Effects of vertical wind shear on the intensity and structure of numerically simulated hurricanes. *Monthly Weather Review*, *128*(9), 2249–2269. https://doi.org/10.1175/1520-0493(2001)129<2249:eovwso>2.0.co;2

Fuglestvedt, H. F., & Haerter, J. O. (2020). Cold pools as conveyor belts of moisture. *Geophysical Research Letters*, *47*(12), e2020GL087319. https://doi.org/10.1029/2020gl087319

Gray, W. M., & Jacobson, R. W., Jr. (1977). Diurnal variation of deep cumulus convection. *Monthly Weather Review*, *105*(9), 1171–1188. https://doi.org/10.1175/1520-0493(1977)105<1171:dvodcc>2.0.co;2

Han, J., & Bretherton, C. S. (2019). TKE-based moist eddy-diffusivity mass-flux (EDMF) parameterization for vertical turbulent mixing. *Weather and Forecasting*, *34*(4), 869–886. https://doi.org/10.1175/waf-d-18-0146.1

Han, J., Wang, W., Kwon, Y. C., Hong, S.-Y., Tallapragada, V., & Yang, F. (2017). Updates in the NCEP GFS cumulus convection schemes with scale and aerosol awareness. *Weather and Forecasting*, *32*(5), 2005–2017. https://doi.org/10.1175/WAF-D-17-0046.1

Harris, L., & Lin, S.-J. (2013). A two-way nested global-regional dynamical core on the cubed-sphere grid. *Monthly Weather Review*, *141*(1), 283–306. https://doi.org/10.1175/mwr-d-11-00201.1

Hazelton, A., Alaka, G. J., Jr., Cowan, L., Fischer, M., & Gopalakrishnan, S. (2021). Understanding the processes causing the early intensification of Hurricane Dorian through an ensemble of the Hurricane Analysis and Forecast System (HAFS). *Atmosphere*, *12*(1), 93. https://doi.org/10.3390/atmos12010093

Hazelton, A. T., Zhang, X., Gopalakrishnan, S., Ramstrom, W., Marks, F., & Zhang, J. A. (2020). High-resolution ensemble HFV3 forecasts of Hurricane Michael (2018): Rapid intensification in shear. *Monthly Weather Review*, *148*(5), 2009–2032. https://doi.org/10.1175/mwr-d-19-0275.1

Hendricks, E. A., Peng, M. S., Fu, B., & Li, T. (2010). Quantifying environmental control on tropical cyclone intensity change. *Monthly Weather Review*, *138*(8), 3243–3271. https://doi.org/10.1175/2010mwr3185.1

Hogsett, W. A., & Stewart, S. R. (2014). Dynamics of tropical cyclone intensification: Deep convective cyclonic "left movers". *Journal of the Atmospheric Sciences*, *71*(1), 226–242. https://doi.org/10.1175/jas-d-12-0284.1

Houze, R. A., Jr. (1997). Stratiform precipitation in regions of convection: A meteorological paradox? *Bulletin of the American Meteorological Society*, *78*(10), 2179–2196. https://doi.org/10.1175/1520-0477(1997)078<2179:spiroc>2.0.co;2

Houze, R. A., Jr. (2004). Mesoscale convective systems. *Reviews of Geophysics*, *42*(4), RG4003. https://doi.org/10.1029/2004rg000150

Iacono, M. J., Delamere, J. S., Mlawer, E. J., Shephard, M. W., Clough, S. A., & Collins, W. D. (2008). Radiative forcing by long–lived greenhouse gases: Calculations with the AER radiative transfer models. *Journal of Geophysical Research*, *113*(D13), D13103. https://doi.org/10.1029/2008jd009944

Jones, S. C. (1995). The evolution of vortices in vertical shear. I: Initially barotropic vortices. *Quarterly Journal of the Royal Meteorological Society*, *121*(524), 821–851. https://doi.org/10.1002/qj.49712152406

Kaplan, J., & DeMaria, M. (2003). Large-scale characteristics of rapidly intensifying tropical cyclones in the North Atlantic basin. *Weather and Forecasting*, *18*(6), 1093–1108. https://doi.org/10.1175/1520-0434(2003)018<1093:lcorit>2.0.co;2

Molinari, J., Dodge, P., Vollaro, D., Corbosiero, K. L., & Marks, F., Jr. (2006). Mesoscale aspects of the downshear reformation of a tropical cyclone. *Journal of the Atmospheric Sciences*, *63*(1), 341–354. https://doi.org/10.1175/jas3591.1

Munsell, E. B., Zhang, F., Sippel, J. A., Braun, S. A., & Weng, Y. (2017). Dynamics and predictability of the intensification of Hurricane Edouard (2014). *Journal of the Atmospheric Sciences*, *74*(2), 573–595. https://doi.org/10.1175/jas-d-16-0018.1

Nesbitt, S. W., & Zipser, E. J. (2003). The diurnal cycle of rainfall and convective intensity according to three years of TRMM measurements. *Journal of Climate*, *16*(10), 1456–1475. https://doi.org/10.1175/1520-0442-16.10.1456

Nguyen, L. T., & Molinari, J. (2015). Simulation of the downshear reformation of a tropical cyclone. *Journal of the Atmospheric Sciences*, *72*(12), 4529–4551. https://doi.org/10.1175/jas-d-15-0036.1

Nguyen, L. T., Molinari, J., & Thomas, D. (2014). Evaluation of tropical cyclone center identification methods in numerical models. *Monthly Weather Review*, *142*(11), 4326–4339. https://doi.org/10.1175/mwr-d-14-00044.1

Python Software Foundation. Python language reference, version 3.8 [Software]. Python. Retrieved from http://www.python.org

Raymond, D. J. (2012). Balanced thermal structure of an intensifying tropical cyclone. *Tellus A*, *64*(1), 19181. https://doi.org/10.3402/tellusa.v64i0.19181

Raymond, D. J., Gjorgjievska, S., Sessions, S., & Fuchs, Z. (2014). Tropical cyclogenesis and mid-level vorticity. *Australian Meteorological and Oceanographic Journal*, *64*(1), 11–25. https://doi.org/10.22499/2.6401.003

Raymond, D. J., & Sessions, S. L. (2007). Evolution of convection during tropical cyclogenesis. *Geophysical Research Letters*, *34*(6), L06811. https://doi.org/10.1029/2006gl028607

Reasor, P. D., Montgomery, M. T., & Grasso, L. D. (2004). A new look at the problem of tropical cyclones in vertical shear flow: Vortex resiliency. *Journal of the Atmospheric Sciences*, *61*(1), 3–22. https://doi.org/10.1175/1520-0469(2004)061<0003:anlatp>2.0.co;2

Rios-Berrios, R., Davis, C. A., & Torn, R. D. (2018). A hypothesis for the intensification of tropical cyclones under moderate vertical wind shear. *Journal of the Atmospheric Sciences*, *75*(12), 4149–4173. https://doi.org/10.1175/jas-d-18-0070.1

Rios-Berrios, R., & Torn, R. D. (2017). Climatological analysis of tropical cyclone intensity changes under moderate vertical wind shear. *Monthly Weather Review*, *145*(5), 1717–1738. https://doi.org/10.1175/mwr-d-16-0350.1

Rios-Berrios, R., Torn, R. D., & Davis, C. A. (2016). An ensemble approach to investigate tropical cyclone intensification in sheared environments. Part I: Katia (2011). *Journal of the Atmospheric Sciences*, *73*(1), 71–93. https://doi.org/10.1175/jas-d-15-0052.1

Rogers, R., Reasor, P., & Lorsolo, S. (2013). Airborne Doppler observations of the inner-core structural differences between intensifying and steady-state tropical cyclones. *Monthly Weather Review*, *141*(9), 2970–2991. https://doi.org/10.1175/mwr-d-12-00357.1

Rogers, R. F., Reasor, P. D., Zawislak, J. A., & Nguyen, L. T. (2020). Precipitation processes and vortex alignment during the intensification of a weak tropical cyclone in moderate vertical shear. *Monthly Weather Review*, *148*(5), 1899–1929. https://doi.org/10.1175/mwr-d-19-0315.1

Rogers, R. F., Zhang, J. A., Zawislak, J., Jiang, H., Alvey, G. R., III, Zipser, E. J., & Stevenson, S. N. (2016). Observations of the structure and evolution of Hurricane Edouard (2014) during intensity change. Part II: Kinematic structure and the distribution of deep convection. *Monthly Weather Review*, *144*(9), 3355–3376. https://doi.org/10.1175/mwr-d-16-0017.1

Ruppert, J. H., Jr., Wing, A. A., Tang, X., & Duran, E. L. (2020). The critical role of cloud–infrared radiation feedback in tropical cyclone development. *Proceedings of the National Academy of Sciences*, *117*(45), 27884–27892. https://doi.org/10.1073/pnas.2013584117

Ryglicki, D. R., Cossuth, J. H., Hodyss, D., & Doyle, J. D. (2018). The unexpected rapid intensification of tropical cyclones in moderate vertical wind shear. Part I: Overview and observations. *Monthly Weather Review*, *146*(11), 3773–3800. https://doi.org/10.1175/mwr-d-18-0020.1

Ryglicki, D. R., Doyle, J. D., Hodyss, D., Cossuth, J. H., Jin, Y., Viner, K. C., & Schmidt, J. M. (2019). The unexpected rapid intensification of tropical cyclones in moderate vertical wind shear. Part III: Outflow–environment interaction. *Monthly Weather Review*, *147*(8), 2919–2940. https://doi.org/10.1175/MWR-D-18-0370.1

Ryglicki, D. R., Hodyss, D., & Rainwater, G. (2020). The tropical cyclone as a divergent source in a background flow. *Journal of the Atmospheric Sciences*, *77*(12), 4189–4210. https://doi.org/10.1175/jas-d-20-0030.1

Schecter, D. A. (2020). Distinct intensification pathways for a shallow-water vortex subjected to asymmetric "diabatic" forcing. *Dynamics of Atmospheres and Oceans*, *91*, 101156. https://doi.org/10.1016/j.dynatmoce.2020.101156

Schecter, D. A. (2022). Intensification of tilted tropical cyclones over relatively cool and warm oceans in idealized numerical simulations. *Journal of the Atmospheric Sciences*, *79*(2), 485–512. https://doi.org/10.1175/jas-d-21-0051.1

Schecter, D. A., & Menelaou, K. (2020). Development of a misaligned tropical cyclone. *Journal of the Atmospheric Sciences*, *77*(1), 79–111. https://doi.org/10.1175/jas-d-19-0074.1

Schubert, W. H., & Hack, J. J. (1982). Inertial stability and tropical cyclone development. *Journal of the Atmospheric Sciences*, *39*(8), 1687–1697. https://doi.org/10.1175/1520-0469(1982)039<1687:isatcd>2.0.co;2

Scofield, R. A. (1990). Instability bursts associated with extratropical cyclone systems (ECSs) and a forecast index of 3–12 hour heavy precipitation.

Smith, R. K., & Montgomery, M. T. (2015). Toward clarity on understanding tropical cyclone intensification. *Journal of the Atmospheric Sciences*, *72*(8), 3020–3031. https://doi.org/10.1175/jas-d-15-0017.1

Smith, R. K., Montgomery, M. T., & Van Sang, N. (2009). Tropical cyclone spin-up revisited. *Quarterly Journal of the Royal Meteorological Society*, *135*(642), 1321–1335. https://doi.org/10.1002/qj.428

Steiner, M., Houze, R. A., Jr., & Yuter, S. E. (1995). Climatological characterization of three-dimensional storm structure from operational radar and rain gauge data. *Journal of Applied Meteorology*, *34*(9), 1978–2007. https://doi.org/10.1175/1520-0450(1995)034<1978:ccotds>2.0.co;2

Tallapragada, V., Bernardet, L., Biswas, M. K., Gopalakrishnan, S., Kwon, Y., Liu, Q., et al. (2014). *Hurricane Weather Research and Forecasting (HWRF) model: 2014 scientific documentation* (p. 105). Developmental Testbed Center. Retrieved from http://www.dtcenter.org/HurrWRF/users/docs/scientific_documents/HWRFv3.6a_ScientificDoc.pdf

Tang, B., & Emanuel, K. (2010). Midlevel ventilation's constraint on tropical cyclone intensity. *Journal of the Atmospheric Sciences*, *67*(6), 1817–1830. https://doi.org/10.1175/2010jas3318.1

Tang, B., & Emanuel, K. (2012). Sensitivity of tropical cyclone intensity to ventilation in an axisymmetric model. *Journal of the Atmospheric Sciences*, *69*(8), 2394–2413. https://doi.org/10.1175/jas-d-11-0232.1

Tang, X., & Zhang, F. (2016). Impacts of the diurnal radiation cycle on the formation, intensity, and structure of Hurricane Edouard (2014). *Journal of the Atmospheric Sciences*, *73*(7), 2871–2892. https://doi.org/10.1175/jas-d-15-0283.1

Tao, C., & Jiang, H. (2015). Distributions of shallow to very deep precipitation–convection in rapidly intensifying tropical cyclones. *Journal of Climate*, *28*(22), 8791–8824. https://doi.org/10.1175/jcli-d-14-00448.1

Tao, D., & Zhang, F. (2019). Evolution of dynamic and thermodynamic structures before and during rapid intensification of tropical cyclones: Sensitivity to vertical wind shear. *Monthly Weather Review*, *147*(4), 1171–1191. https://doi.org/10.1175/mwr-d-18-0173.1

Trabing, B. C., & Bell, M. M. (2020). Understanding error distributions of hurricane intensity forecasts during rapid intensity changes. *Weather and Forecasting*, *35*(6), 2219–2234. https://doi.org/10.1175/waf-d-19-0253.1

Wang, X., & Jiang, H. (2021). Contrasting behaviors between the rapidly intensifying and slowly intensifying tropical cyclones in the North Atlantic and eastern Pacific basins. *Journal of Climate*, *34*(3), 987–1003. https://doi.org/10.1175/jcli-d-19-0908.1

Zawislak, J., Jiang, H., Alvey, G. R., Zipser, E. J., Rogers, R. F., Zhang, J. A., & Stevenson, S. N. (2016). Observations of the structure and evolution of Hurricane Edouard (2014) during intensity change. Part I: Relationship between the thermodynamic structure and precipitation. *Monthly Weather Review*, *144*(9), 3333–3354. https://doi.org/10.1175/mwr-d-16-0018.1

Zawislak, J., Rogers, R. F., Aberson, S. D., Alaka, G. J., Jr., Alvey, G. R., III, Aksoy, A., et al. (2022). Accomplishments of NOAA's airborne hurricane field program and a broader future approach to forecast improvement. *Bulletin of the American Meteorological Society*, *103*(2), E311–E338. https://doi.org/10.1175/bams-d-20-0174.1

Zhang, X., & Xu, W. (2021). Diurnal variations in rainfall and precipitation asymmetry of tropical cyclones in the northwest Pacific region. *Journal of Climate*, *34*(13), 5565–5582. https://doi.org/10.1175/jcli-d-20-0795.1

Zhou, L., Lin, S.–J., Chen, J.–H., Harris, L. M., Chen, X., & Rees, S. L. (2019). Toward convective–scale prediction within the next generation global prediction system. *Bulletin of the American Meteorological Society*, *100*(7), 1225–1243. https://doi.org/10.1175/bams-d-17-0246.1